Gas Shale Permeability and Velocity Measurement at Laboratory Scale

---

A Thesis Presented to

the Faculty of the Department of Earth and Atmospheric Sciences

University of Houston

In Partial Fulfillment

of the Requirements for the Degree

Master of Science

By

Kefei Lu

November 2012

Gas Shale Permeability and Velocity Measurement at Laboratory Scale

_____

Kefei Lu

APPROVED:

_____

Dr. Evgeny M. Chesnokov, Chairman
Department of Geosciences

_____

Dr. John Castagna
Department of Geosciences

_____

Dr. Yasser M. Metwally
Department of Geosciences

_____

Mr. Dana Jurick
Devon Energy Corporation

_____

Dean, College of Natural Science and Mathematics

ACKNOWLEDGEMENTS

I would like to thank my advisor Dr. Evgeny M. Chesnokov and my committee members Dr. John Castagna, Mr. Dana Jurick, and Dr. Yasser M. Metwally for their guidance, valuable remarks, and corrections.

Dr. Evgeny M. Chesnokov, my dissertation supervisor, has provided guidance and contributed many useful suggestions to this dissertation. I appreciate his patient instruction on this dissertation. I want to thank Dr. Yasser M. Metwally, my dissertation co-advisor, for his advice and guidance on my work in the lab. I also want to thank Dr. John Castagna and Mr. Dana Jurick for their useful comments, suggestions, and encouragement in my study. Special thanks extend to Dr. Nikolay Dyaur for his help and technique support on the ultrasonic velocity measurement.

Gas Shale Permeability and Velocity Measurement at Laboratory Scale

---

An Abstract of a Thesis

Presented to

the Faculty of the Department of Earth and Atmospheric Sciences

University of Houston

In Partial Fulfillment

of the Requirements for the Degree

Master of Science

By

Kefei Lu

November 2012

ABSTRACT

Matrix permeability of gas shales is a crucial parameter for their characterization, production potential, and commercial development. Gas shales are an important reservoir type from an economic perspective because of their potential to hold large volume reserves and produce economically over time. However, shale matrix permeability can not be easily acquired from direct field measurements; it can only be measured in the laboratory.

The main goal of this thesis was to characterize the elastic properties and gas transport properties for the Barnett shale which comes from the Fort Worth basin in North Texas, of the United States. We measured density and ultrasonic velocity based on the three plug technique. Matrix permeability and porosity were measured simultaneously by using a specially designed apparatus and a newly developed transient pressure technique invented by Metwally and Sondergeld, 2011.

Measurement results show evidence for strong anisotropy in both velocity and permeability attributes. Nonlinear reduction in permeability and effective porosity with an increase of effective pressure has been observed. Correlation between elastic constant C44 and permeability parallel to the bedding plane has been clearly identified, which may offer an indicator for estimating permeability.

CONTENTS

LIST of TABLES

LIST of FIGURES

Chapter 1 Introduction

1.1 Importance of shale

Shale is a fine-grained, organic-rich, sedimentary rock characterized by thin layers of clay and mud. It is the most abundant of the sedimentary rocks in the crust of the Earth (Pettijohn, 1975). In petroleum geology, organic shales are source rocks as well as seal rocks that trap oil and gas. In reservoir engineering, shales are flow barriers. In drilling, the bit often encounters more shale than reservoir sandstones. In seismic exploration, shales are seismic reflectors (Wang, 2002). As a result, seismic and petrophysical properties of shales and the relationships among these properties are important for both exploration and reservoir management (Wang, 2002).

It's known that shale can be the source, reservoir, and seal for natural gas. Since 2000, rapid growth in the production of natural gas from shale formations in the North America has made shale reservoirs a substantial new energy resource. Through new drilling and completion engineering technology and techniques invented to develop these reservoirs economically, natural gas resource estimates have grown significantly in the past decade (Energy Information Administration, 2010). In the United States, some of the largest gas reservoirs, like the Barnett Shale of Texas and the Marcellus Shale of the northeast U.S., are capable of producing many million cubic feet of gas per day by using horizontal drilling and hydraulic fracturing completion engineering

technology.

1.2 Motivation

Gas shales are considered an unconventional gas resource type of reservoir (permeability less than 0.1 mDarcy). As unconventional gas reservoirs, the fluid flow and elastic properties of these shales are critical to identify the reservoir's production and recovery potential. However, data on gas shales' elastic properties and permeability are very scarce because it's hard to obtain and preserve shale samples and the measurement is very difficult and time consuming due to their low permeability.

Permeability is an important parameter for predicting reservoir production. Many researches have focused on measuring matrix permeability in laboratory and improving the accuracy of its measurement. Based on this, the present study uses a modified pressure pulse decay technique to measure matrix permeability on shale core plugs, and identifies systematic errors in these types of measurements and provides recommendations on how they can be minimized.

It is important to note that fluid flow and elastic wave propagation in rocks are different mechanisms. However, we know that fluid flow can cause attenuation of elastic wave and the texture of clay layering and the shape of connected channels may also contribute not only to the permeability anisotropy, but also to the elastic property anisotropy. Anisotropy means that measured dependent upon and sensitive to the

orientation and direction from which the measurement is made across a sample of physical material. To find the relationship between these two different mechanisms, fluid flow and elastic wave propagation, we will measure both the permeability and the ultrasonic wave velocity of oriented samples in the laboratory.

In general, the motivation of this thesis is to measure elastic properties and matrix permeability of tight gas shale at the laboratory scale and develop related experimental techniques in an effective and accurate way.

1.3 Sample introduction

The shale samples studied in this work are from the Barnett Shale formation that derived from the Fort Worth Basin in North Central Texas (Figure1-1). It is one of the largest and most active domestic natural gas plays in the U.S. The play could be quite large, potentially spanning 10-15 counties in the Fort Worth Basin of north Texas (the shale is bordered to the east by the Ouachita Thrust-fold Belt and the Muenster Arch and to the west by the Bend Arch).

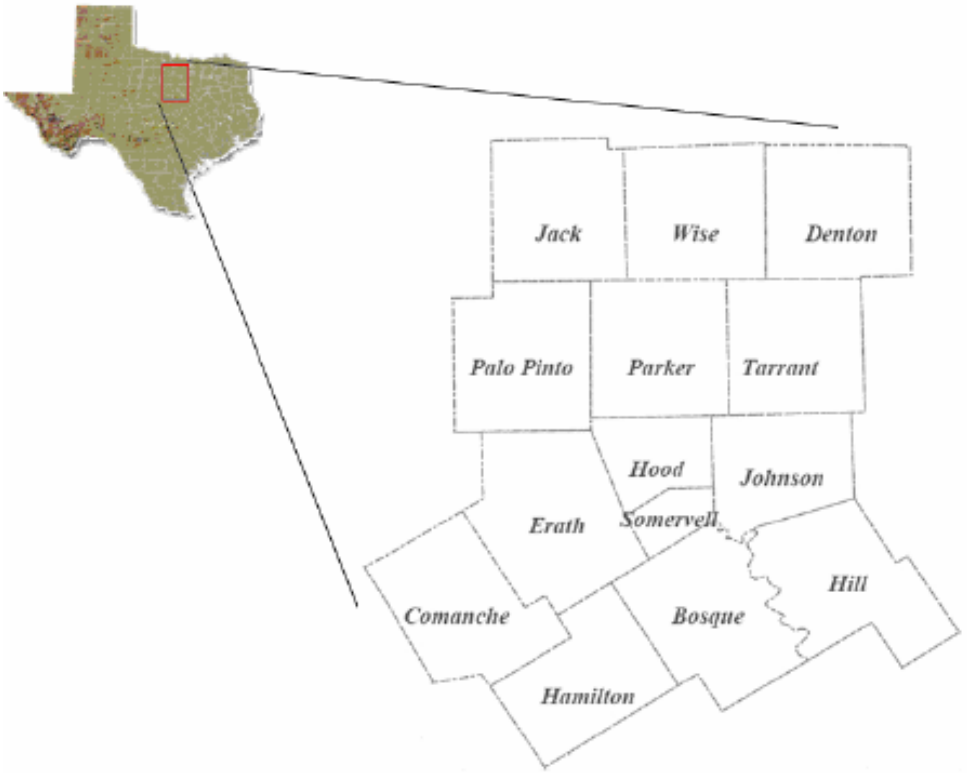

Figure 1-1: Barnett Shale producing counties in the Fort Worth Basin. (*Source: Humble Geochemical, Pickering Energy Partners.*)

The Barnett Shale formation is a Mississippian-aged shale located at depths of 6,500-8,500 feet below surface. Figure 1-2 shows the stratigraphy of the Fort Worth Basin. The Barnett lies between two limestone units, the underlying Ordovician-age Viola limestone formation and the overlying Pennsylvanian-age Marble Falls limestone formation. In the northeast portion of the Barnett "play area", the Barnett is split into the upper and lower Barnett by the Forestburg limestone.

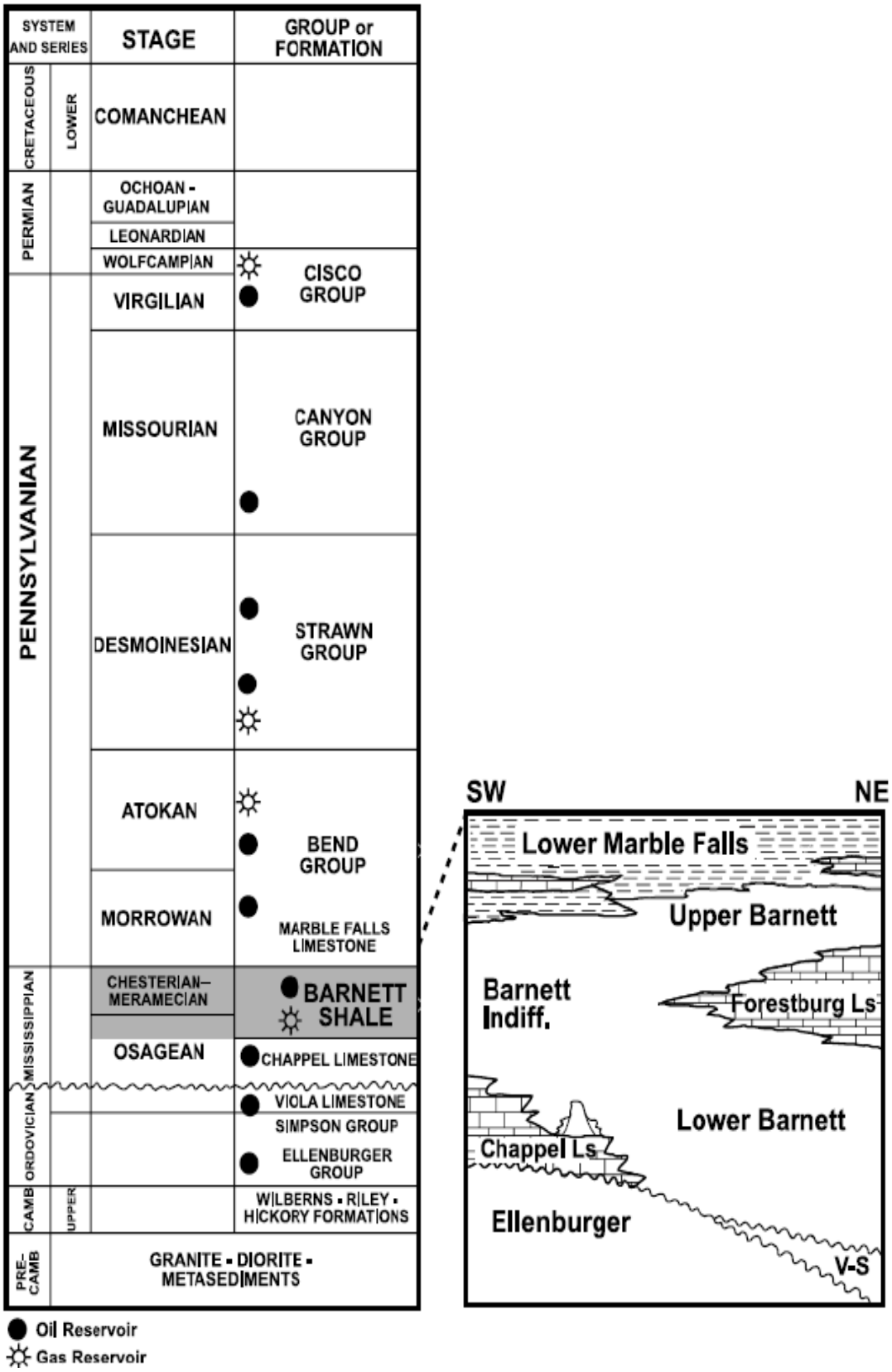

Figure 1-2: Generalized stratigraphy section of the Bend arch – Fort Worth Basin showing the distribution of source, reservoir, and seal rocks of the Barnett- Paleozoic total petroleum system (TPS). (*Picture from the American Association of Petroleum Geologists*)

We received a total of twelve core samples drilled from six wells that were located in five counties in the Fort Worth Basin (Table 1-1). Two cores were taken at different depth for each well in the sample set.

Table 1-1: Barnett Shale core samples

No.	Well Name	County	State	Depth (ft)	Sample No.
1	AS-lower	Wise	TX	xx86	A
2	AS-upper	Wise	TX	xx86	B
3	ST-upper	Parker	TX	xx05	C
4	ST-lower	Parker	TX	xx05	D
5	JR-upper	Denton	TX	xx91	E
6	JR-lower	Denton	TX	xx18	F
7	RS-upper	Johnson	TX	xx30	G
8	RS-lower	Johnson	TX	xx30	H
9	BR-lower	Tarrant	TX	xx90	I
10	BR-upper	Tarrant	TX	xx80	J
11	SC-lower	Wise	TX	xx90	K
12	SC-upper	Wise	TX	xx91	L

1.4 Overview of thesis

This study is divided into four parts. Chapter 2 describes the techniques used for measuring ultrasonic velocity. Chapter 3 describes the techniques used for measuring matrix permeability. Chapter 4 reports the results measured and the analysis of all the measurements, and Chapter 5 gives the overall summary and conclusions of this research.

Chapter 2 Ultrasonic Velocity and Anisotropy

2.1 Three plugs technique and sample preparation

Shale with bedding planes are generally taken as elastic media of transverse isotropy (TI). A transversely isotropic rock has a hexagonal symmetry with five independent elastic constants (Love, 1927). The symmetry axis of isotropy is normally perpendicular to the bedding plane. In order to measure transversely isotropy completely, core plugs in three directions must be measured separately to derive the five independent elastic constants. The three plugs technique of velocity measurement in the laboratory is showed in figure below.

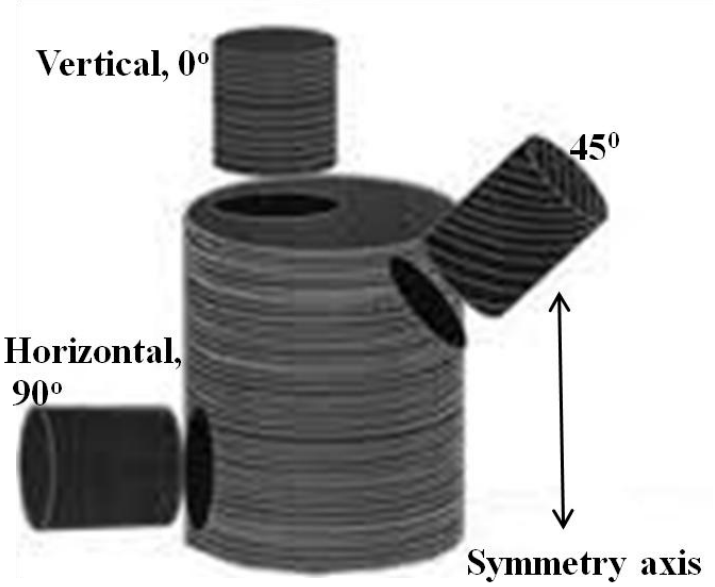

Figure 2-1: Three-plug method for measuring transverse isotropy in laboratory core samples (*after Wang, 2002*). Cylindrical sample is cut from three directions, normal to the bedding, parallel to bedding and diagonal to bedding at 45 degrees to the symmetry axis.

Three adjacent one inch diameter plugs are cut from four inch diameter core: one vertical, one horizontal, and one 45 degrees to the symmetry axis. Nine velocities are measured, three in each direction, one compressional and two shear waves. All three waves propagate parallel to the plug axis; the polarizations of the two shear waves are orthogonal to each other and in a plane that is normal to the plug axis. Figure 2-2 shows in more detail the particle polarizations and the direction of propagation of these waves.

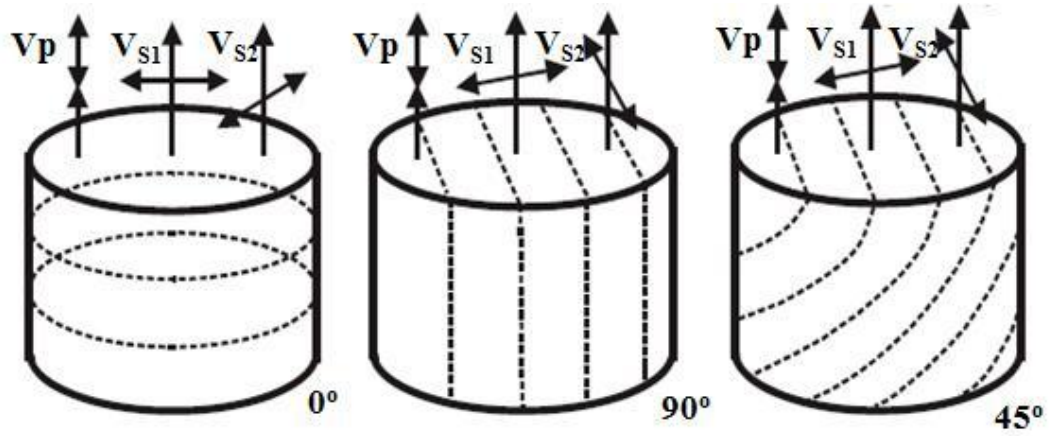

Figure 2-2: Schematic diagrams for nine velocities measured in the experiment. The single arrow represents the directions of wave propagation, double arrows represent the polarization of the particle and dashed lines in the samples represent bedding planes (*after Deng et al., 2009*). Zero degree is plug cut perpendicular to the bedding plane, 90 degree is plug cut parallel to the bedding plane and 45 degree is plug cut at a 45 degree angle to the symmetry axis

The length of the plugs is less than two inches (permeability measurement equipment limitation). The two ends of each plug are polished carefully to make sure they are parallel to each other and perpendicular to the plug axis, which is an important step in order to measure the ultrasonic velocity accurately.

The density of each plug comes from the results of the weight and bulk volume measurement. The bulk volume is obtained from their geometry dimensions as they have regular cylindrical configurations. Note that the mercury immersion method is more accurate than the method of calculating the bulk volume from plug dimensions, because it avoids the errors coming from dimensions measurement. With these values we can calculate the bulk density of each core plugs.

Together with the velocities and densities measured on the three core plugs, the elastic constants C11 and C66, C33 and C44, and C13 can be derived (Appendix A).

$$C_{33} = \rho V_{p0}^2 \tag{2-1}$$

$$C_{11} = \rho V_{p90}^2 \tag{2-2}$$

$$C_{44} = \rho V_{S1,90}^2 \tag{2-3}$$

$$C_{66} = \rho V_{S2,90}^2 \tag{2-4}$$

$$C_{13} = \left[\frac{\left(4\rho V_{P,45}^2 - C_{11} - C_{33} - 2C_{44}\right)^2 - (C_{11} - C_{33})^2}{4}\right]^{\frac{1}{2}} - C_{44} \tag{2-5}$$

Meanwhile, the Thomsen anisotropy parameters (1986) ε, γ, and δ also can be calculated from the derived elastic constants.

$$\varepsilon = \frac{C_{11} - C_{33}}{2C_{33}} \tag{2-6}$$

$$\gamma = \frac{C_{66} - C_{44}}{2C_{44}} \tag{2-7}$$

$$\delta = \frac{2\left(C_{13} + C_{44}\right)^2 - (C_{33} - C_{44})\left(C_{11} + C_{33} - 2C_{44}\right)}{2C_{33}^2} \tag{2-8}$$

2.2 Pulse transmission technique and experiment setup

The ultrasonic velocity (V) of core plugs is calculated by the interval transit time (T) which is an ultrasonic P- or S-wave travel time through a core plug with certain length (L),

$$V = \frac{L}{T - T_d} \tag{2-9}$$

Where, T_d is the system delay time, which is measured by picking the first break of the signal when the transducers were placed together head to head. The travel time of each wave type through the sample is calculated by subtracting the delay time from the time of wave propagating through the sample, which can be obtained from the first break of the signal. Then velocity is calculated by using equation 2-9. The length of the core plug is measured with a length gauge.

The pulse transmission technique used for the ultrasonic velocity experiment includes pulse/receiver, piezoelectric transducer, and display devices. A pulse/receiver is an electronic device that can produce high voltage electrical pulses. The piezoelectric transducer can then generate high frequency ultrasonic energy driven by the pulse. The acoustic energy is introduced and propagates through the samples in the form of waves. The reflected wave signal is transformed into an electrical signal by the transducer and is displayed on a screen and recorded as a seismogram.

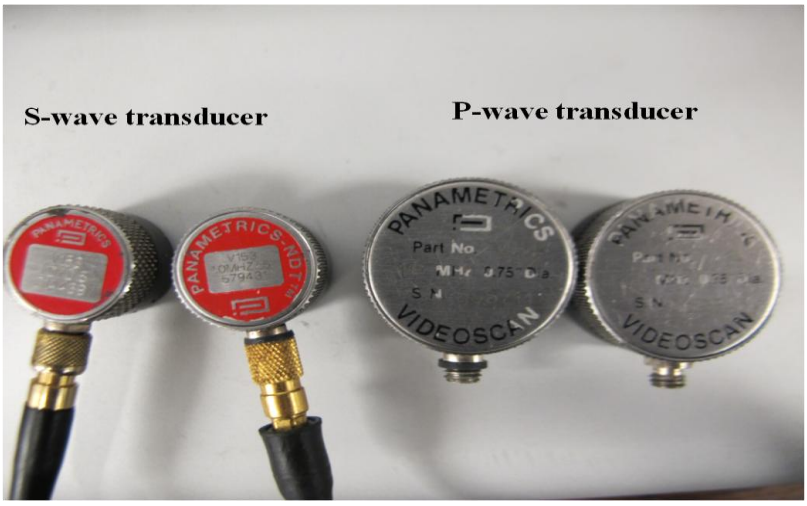

Figure 2-3: Photo of P-wave and S-wave piezoelectric transducer with central frequency of 1MHz

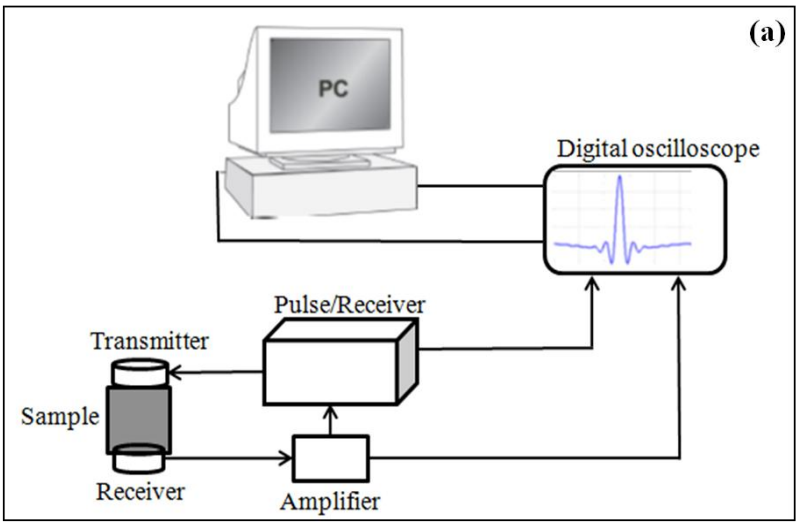

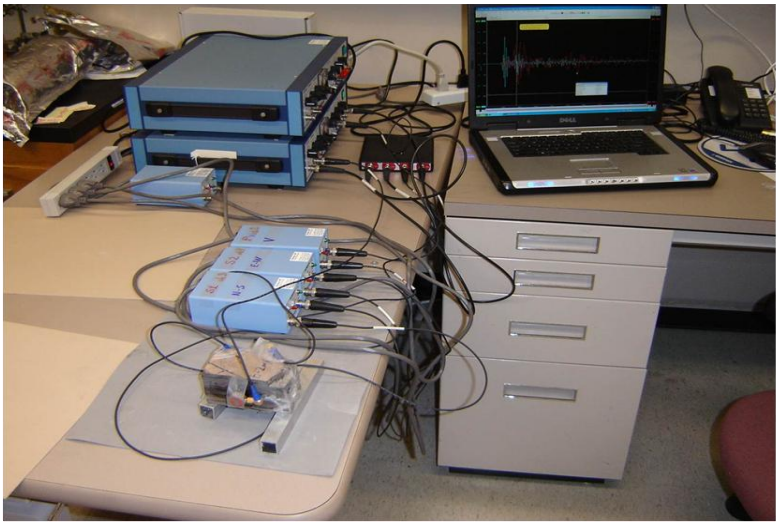

Figure 2-4: Schematic diagram of experiment setup. a) Schematic diagram of the pulse transmission technique, b) Photo of the whole system (*picture from Dr. Nikolay Dyaur*)

2.3 Uncertainty of ultrasonic velocity measurement

To measure velocity, we employed the pulse transmission technique. The digital oscilloscope to record the waveforms had sampling rate of 50 MHz and allowed us to make first arrival pick times within an uncertainty bound of +/-20 ns. The central frequency of P-waves and S-waves piezoelectric transducers was 1MHz. According to the velocity equation 2-9, the error bar of ultrasonic velocity ΔV can be derived as,

$$\frac{\Delta V}{V} = \sqrt{\left(\frac{\Delta T}{T}\right)^2 + \left(\frac{\Delta L}{L}\right)^2} \qquad (2\text{-}10)$$

Where ΔT and ΔL are the errors from picking time and measuring the length of the core plugs. The accuracy of velocity measurements for P-wave was about 1%, and for S-wave was around 2%, depending on the polarization of shear waves.

Chapter 3 Gas Permeability Measurement

3.1 Permeability introduction

Permeability is a measureable parameter indicating the ability of a porous media to transport fluid under a pressure gradient. In 1856, Henry Darcy published the relationship between the discharge flux q through porous media under the pressure gradient $\Delta P/L$ which is proportionally dependent upon the permeability of the medium *k*, which is known as Darcy's Law.

$$q = k\frac{\Delta p}{L} \tag{3-1}$$

In the 1950's, permeability was considered to be a property of the porous media only, so it should be independent of the kind of fluid flowing through it (Hubbert, 1957). Therefore, viscosity μ was separated from the proportional constant as a variation of Darcy's Law,

$$q = \frac{k}{\mu}\frac{\Delta p}{L} \tag{3-2}$$

where *k* is permeability.

In general, two different types of permeability can be observed in shale gas reservoirs: fracture permeability and matrix permeability. Fracture permeability is the capability that fluid flows through the natural fractures in the shale, as well as from fractures created or "stimulated" through hydraulic-fracturing. Matrix permeability is

the capability that fluid flows through the intact portion of the shale (the matrix). Fracture permeability is usually in the millidarcy range (Bustin et al., 2008), however matrix permeability of shale is in the range from microdarcy to nanodarcy (Bustin, 2005). Even though matrix permeability is much lower than fracture permeability, it controls the production of a shale gas reservoir (Luffel et al., 1993; Bustin et al., 2008). This study will focus on the matrix permeability and the experimental methods that are used to measure it.

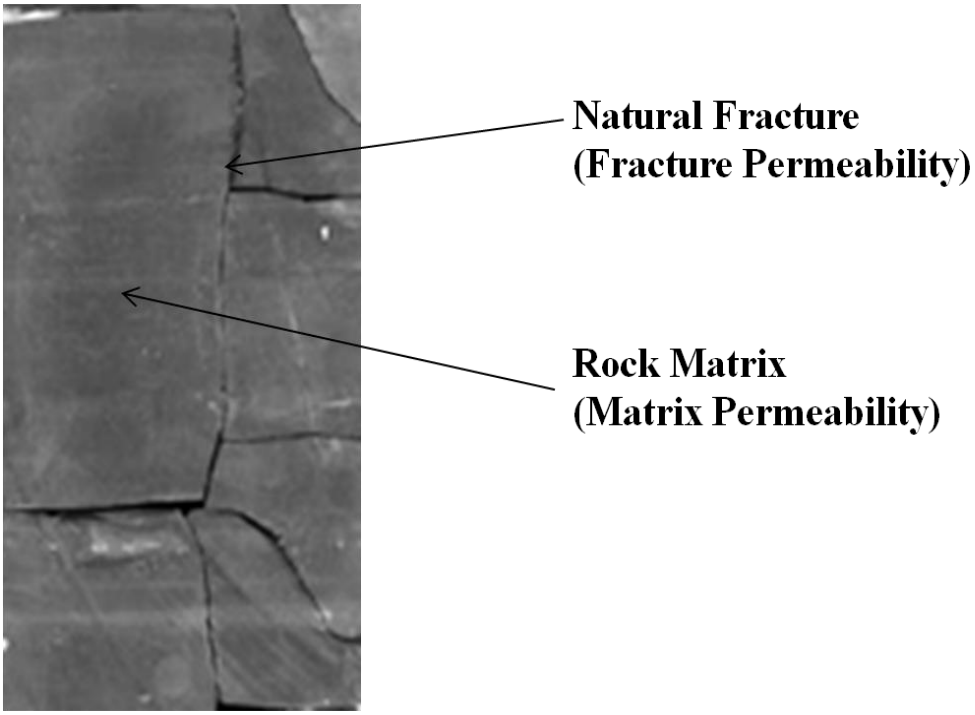

Figure 3-1: Fracture permeability and matrix permeability characteristic different fluid transportation ability at different areas in rock reservoirs. Picture (*modified from Gale et al., 2007*) is core of Barnett Shale from Fort Worth basin.

3.2 Permeability tensor

The permeability of gas shale has a directional dependency, which means the permeability measured normal to shale bedding planes is usually different from that parallel-to-bedding planes. Thus, permeability can be considered as a second rank tensor and has the form (Metwally and Chesnokov, 2010),

$$k = \begin{pmatrix} k_{xx} & k_{xy} & k_{xz} \\ k_{yx} & k_{yy} & k_{yz} \\ k_{zx} & k_{zy} & k_{zz} \end{pmatrix} \tag{3-3}$$

In the principal coordinate system, the off-diagonal terms are absent, and the tensor becomes

$$k = \begin{pmatrix} k_{xx} & 0 & 0 \\ 0 & k_{yy} & 0 \\ 0 & 0 & k_{zz} \end{pmatrix} \tag{3-4}$$

For a TI medium $k_{xx} = k_{yy}$ or $k_{xx} = k_{zz}$ or $k_{yy} = k_{zz}$ depending on the orientation of the symmetry axis. Generally, if the diagonal components of the permeability tensor are known, the permeability for any direction specified by the direction cosines n_x, n_y, n_z is calculated by the formula (Heinbockel 2001):

$$k^{(n)} = k_{ij} n_i n_j = k_{xx} n_x^2 + k_{yy} n_y^2 + k_{zz} n_z^2 \tag{3-5}$$

For TI media such as shale, $k_{xx} = k_{yy} \neq k_{zz}$, if the vertical axis is perpendicular to the bedding plane. Then the equation can be simplified as,

$$k^{(n)} = k_{xx}\left(n_x^2 + n_y^2\right) + k_{zz} n_z^2 \tag{3-6}$$

This means, that for shale, we only need to measure the permeability parallel to bedding and perpendicular to bedding to reconstruct the permeability tensor for a sample. In order to verify the theoretical approach for building up permeability tensor, permeability in the 45^0 direction is included in our measurements.

3.3 Permeability determination and pressure-transmission technique

The standard technique of measuring permeability on rock samples from conventional oil or gas reservoirs are steady-flow techniques (American Petroleum Institute (API) 1998). However, the conventional method is impractical to measure the permeability of very tight rocks, like gas shale (or unconventional reservoir rocks with permeability less than 0.1 mD), because the low flow rates across the core plug are hard to measure and to control, and it also requires a very long time to establish a steady-state flow. In 1968, Brace et al. developed a non-steady-state technique known as pressure-pulse decay or transient-flow technique. Following the original work of Brace et al., Hsieh et al. (1981) and Dicker and Smits (1988) derived the general solution for the pressure difference between samples as a function of time. Jones (1997) took into account of the storage capacity of core sample in the general solution and minimized the errors of the methods. Bustin et al. (2008, 2009) presented the solution for gas adsorption and gas diffusion effect which may result in non-systematic error. Metwally and Sondergeld (2011) used a modified transient-flow technique to overcome the gas adsorption problem and increased accuracy, which is the method used in this study.

In the pressure-pulse decay technique, a confined core sample is set up to connect two fluid reservoirs (Figure 3-2). The volume and pressure for both upstream and downstream fluid reservoirs are known. Then a pressure pulse is added on the upstream fluid reservoir. Pressure differences between the two reservoirs forces the

fluid to flow across the sample. With time the pressure difference starts to decay based on the sample permeability. Recording the pressure decay with time provides the ability to calculate permeability (Brace et al., 1968; Hsieh et al., 1981; Dicker and Smits, 1988; Jones, 1997).

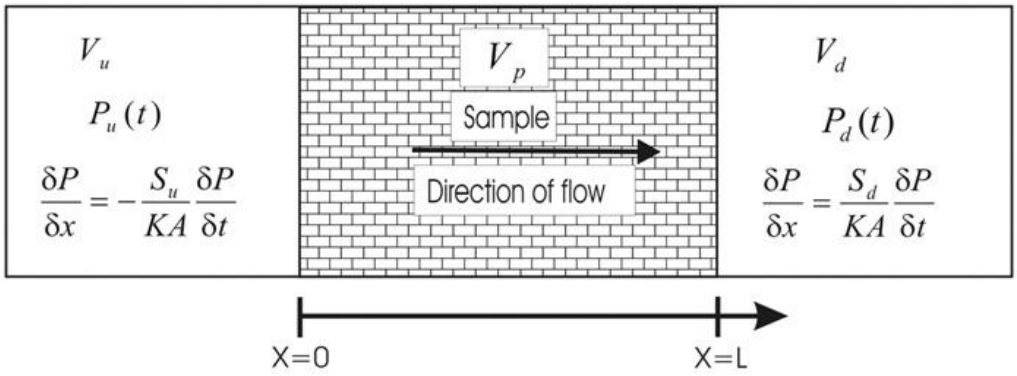

Figure 3-2: Schematic diagram of pressure pulse decay experiment with pressure gradient applied between the upstream and downstream reservoirs. Upstream is using the subscript u and downstream has the subscript d (*Metwally and Sondergeld, 2011*).

The general governing equation that describes pressure change in one dimension along the axis of the cylindrical sample is based on Darcy's law and mass conservation equation and can be described as follow:

$$\frac{\partial^2 P}{\partial x^2} = \frac{S_s}{K}\frac{\partial P}{\partial t} \qquad \text{for} \quad 0 < x < L \text{ and } t > 0 \tag{3-7}$$

With initial and boundary conditions:

$$P(x, 0) = P_d(0) \qquad \text{for} \quad 0 < x < L, \tag{3-8a}$$

$$P(0, t) = P_u(t) \qquad \text{for} \quad t \geq 0, \tag{3-8b}$$

$$P(L, t) = P_d(t) \qquad \text{for} \quad t \geq 0, \tag{3-8c}$$

$$\left(\frac{\partial P_u}{\partial x}\right)_{x=0} = -\frac{S_u}{KA}\frac{\partial P}{\partial t} \qquad \text{for} \quad t > 0 \tag{3-8d}$$

and

$$\left(\frac{\partial \mathrm{P_d}}{\partial \mathrm{x}}\right)_{x=L} = \frac{S_d}{KA}\frac{\partial P}{\partial t} \qquad \text{for } t > 0 \qquad \text{(3-8e)}$$

where P (MPa) is the pressure, t (s) is the time after the pressure is applied, A (m^2) is the cross-section area, K is the hydraulic conductivity, which depends on the fluid properties and sample permeability, and is expressed as,

$$\mathrm{K} = \frac{k\rho g}{\mu} \qquad \text{(3-9)}$$

where k is the permeability (m^2), ρ is the density of the fluid (kg/m^3), g is the gravitational acceleration (m/s^2), μ is the viscosity of the fluid (Pa.s). And Ss is the specific storage of the sample, which can be specified according to Walsh (1965) as,

$$S_s = (\beta_{eff} - \beta_s) + \emptyset_e(\beta_f - \beta_s) \qquad \text{(3-10)}$$

where β_f is the static compressibility of the fluid (atm^{-1}), β_{eff} is the effective compressibility of the rock (atm^{-1}), β_s is the compressibility of the solid matrix (atm^{-1}), and $\emptyset_e$ is the connected porosity of the sample (fraction).

Brace et al. (1968) assumed that the porosity $\emptyset_e$ is very small and both β_{eff} and β_s are very small compared with β_f, based on the rock sample he tested is granite, i.e. he assumed that there is no compressive storage in the rock sample. So the pressure distribution reduces to,

$$\frac{\partial^2 P}{\partial \mathrm{x}^2} = 0 \qquad \text{(3-11)}$$

And

$$\frac{\partial P}{\partial x} = f(t) \qquad \text{(3-12)}$$

The pressure gradient in the sample is constant along the sample length but will vary with time. Brace et al. (1968) derived that the pressure gradient decays exponentially to zero and the upstream pressure is given by the equation,

$$(P_u - P_{final}) = \Delta P[(V_d/V_u) + V_d]e^{-\alpha t} \quad (3\text{-}13)$$

where,

$$-\alpha = \frac{-kA}{\beta_f \mu L}\left(\frac{1}{V_u} + \frac{1}{V_d}\right) \quad (3\text{-}14)$$

P_{final} is the final pressure after the pressure gradient decays to zero, and $\delta P = P_u(0) - P_d(0)$ is the change of pressure in reservoirs at time = 0. By plotting the pressure decay (P_u - P_{final}) on semi-log paper against time, we can get the slop $-\alpha$ of the resulting line and use it to calculate the permeability k from equation 3-14. Examples are shown as below,

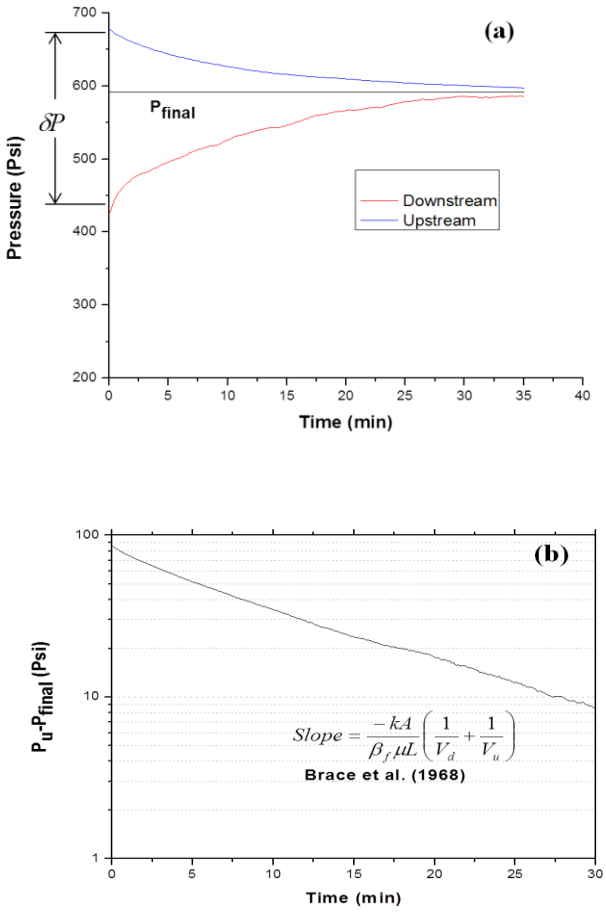

Figure 3-3: (a) Changes of pressure between upstream and downstream reservoirs over time by using technique presented by Brace et al. (1986). (b) Permeability calculated by using the slope of pressure decay against time.

For most of crystalline rocks, the assumption of ignoring porosity and compressibility of rock sample suggested by Brace et al. (1968) may be reasonable but it may not be true for sedimentary rocks like shale, because those rocks usually have significant compressive storage capacity. Taking the compressive storage of rock sample into account, Hsieh et al. (1981) and Dicker and Smits (1988) presented a general analytical solution for the dimensionless pressure difference (δP_D) as a function of dimensionless time,

$$\delta P_D = 2\sum_{n=1}^{\infty} \frac{a(b^2+\theta_n^2) - (-1)^n b\sqrt{(a^2+\theta_n^2)(b^2+\theta_n^2)}}{\theta_n^2(\theta_n^2+a+a^2+b+b^2)+ab(a+a+ab)} \times e^{(-\theta_n^2 t_D)} \tag{3-15}$$

where θ_n is the *n*th root of the equation,

$$\tan\theta = \frac{(a+b)\theta}{\theta^2-ab} \tag{3-16}$$

and *a* and *b*, the ratios of the sample pore volume V_p to the upstream reservoir volume V_u and the downstream reservoir volume V_d,

$$\mathrm{a} = \frac{V_p}{V_u} \qquad \text{and} \qquad \mathrm{b} = \frac{V_p}{V_d} \tag{3-17}$$

δP_D is the normalized dimensionless pressure difference,

$$\delta P_D = \frac{P_u(t)-P_d(t)}{P_u(0)-P_d(0)} \tag{3-18}$$

and the dimensionless time t_D is given by,

$$t_D = \frac{kt}{\beta_f \emptyset_e \mu L^2} \tag{3-19}$$

The compressibility of rock matrix is also ignored because it is relatively small compared with the fluid compressibility.

When gas shales are taken into account, several factors will affect the pressure decay procedure along the sample length. One of the factors needs to be considered is the heterogeneity of shale. The slope of differential pressure change with time will be sensitive to the heterogeneity of shale sample, which will lead to an erroneous calculation of permeability indicated by Kamath et al. (1992). Another factor interfering with the accuracy of the permeability measurement is gas adsorption for the shale. When gas flows through the rock plug, some of the gas molecules will be adsorbed onto the surface of the organic matter due to the negative electrical charges on the surface area and shales are known to be organic-rich sedimentary rock. Bustin et al. (2009) derived that the permeability would be underestimated in case of gas adsorption.

To solve the problems mentioned above, Metwally and Sondergeld (2011) suggested a method by creating an infinite storage capacity for the upstream reservoir and recording the pressure build-up for downstream. This technique makes the upstream pressure constant and the pressure difference decays only when the pressure at the end of the sample changes. As the pressure build up at the downstream is created by the fluid, it actually goes through the core sample, and it can avoid the influence on pressure decay along the core sample due to shale heterogeneity and gas adsorption. In addition, by ignoring the volume of upstream reservoir this method also can avoid the error that is related to the volume measurement. We use this method in our study to measure the gas shale permeability.

When the upstream volume is assumed to be infinite by keeping a constant pressure, parameter "a" in equation 3-17 becomes zero and equation 3-15 becomes,

$$\delta P_D = 2\sum_{n=1}^{\infty} \frac{-(-1)^n b\sqrt{\theta_n^2(b^2+\theta_n^2)}}{\theta_n^2(\theta_n^2+b+b^2)} \times e^{(-\theta_n^2 t_D)} \qquad (3\text{-}20)$$

where θ_n is the *n*th root of below equation,

$$\tan\theta = \frac{b}{\theta} \qquad (3\text{-}21)$$

the value of θ can be derived for different value of b, see below Figure 3-4,

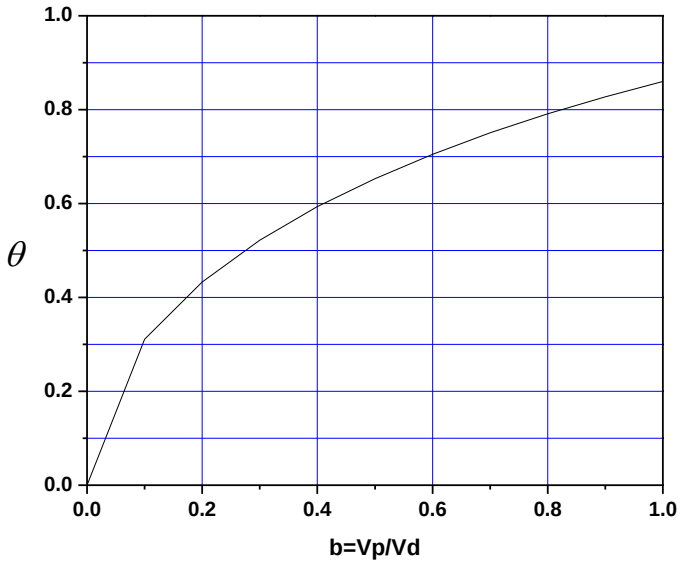

Figure 3-4: Relationship between b and θ for the current permeability measurement system.

As discussed by previous researches (Dicker and Smits 1988; Jones 1997), the solution of equation 3-20 can be approximated a single-exponential of time and can be simplified as,

$$\ln\big(\delta P(t)\big) = \ln(f_1) + \left(-\frac{\theta^2 k}{\beta_f \emptyset_e \mu L^2}\right) t \qquad (3\text{-}22)$$

So, if we know the slope of the logarithm of normalized pressure against time, the permeability can be calculated as,

$$\text{Slope} = \frac{\ln(\delta P(t_n)/\delta P(t_0))}{t_n - t_0} = -\frac{\theta^2 k}{\beta_f \emptyset_e \mu L^2} \quad (3\text{-}23)$$

Examples are shown in figure 3-5,

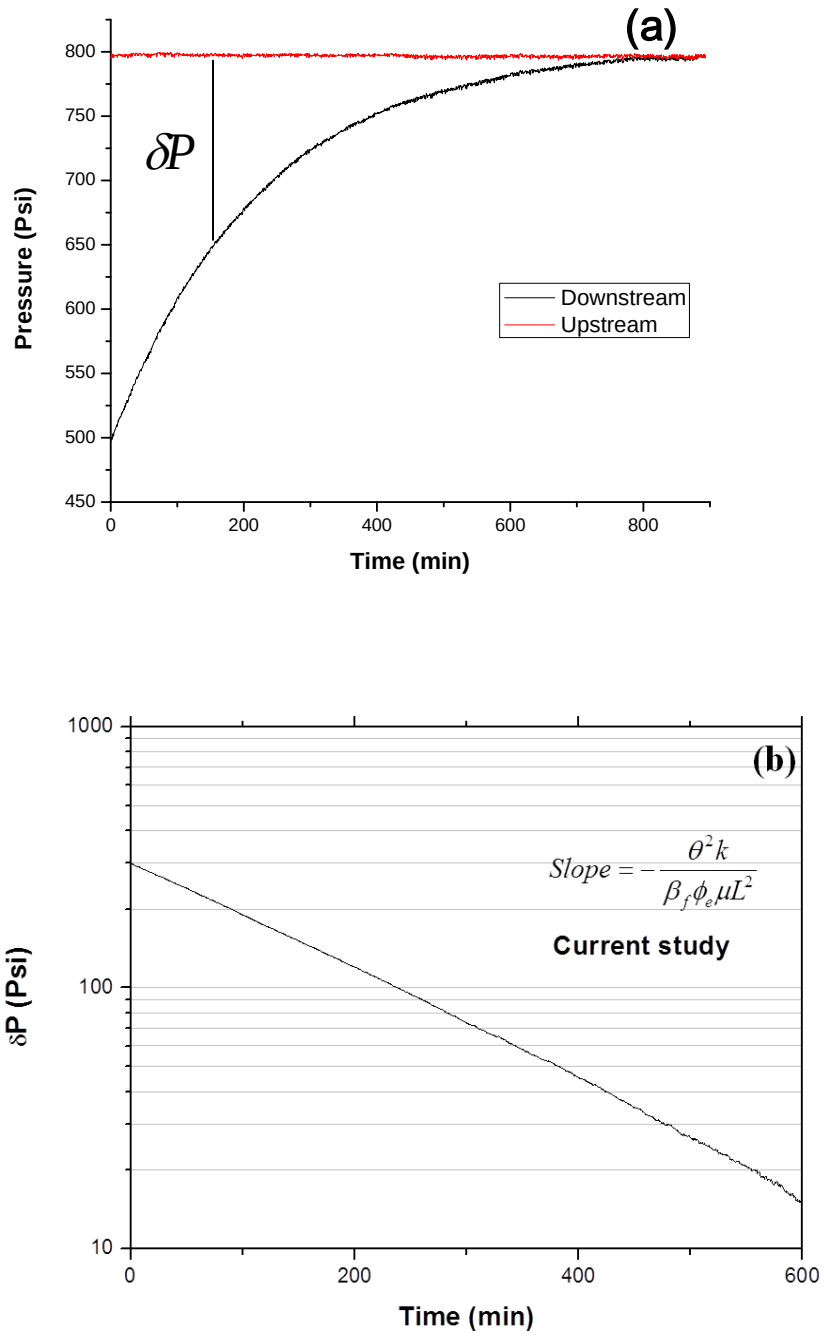

Figure 3-5: (a) Changes of pressure change between upstream and downstream reservoirs over time by using current technique. (b) Permeability calculated by using the slope of differential pressure changing against time.

3.4 Permeability measurement setup

The apparatus used in the permeability measurement is specially designed to allow simultaneous measurement of permeability and porosity under the same conditions of confining pressure, pore pressure, and temperature. The apparatus has three hydrostatic pressure vessels and they are controlled by three syringe pumps (see below Figure 3-6). These pumps have cylinder capacity of $103 \times 10^{-6}\ m^3$ ($0.01 \times 10^{-9}\ m^3$ accuracy) and can maintain hydrostatic pressure to 10,000 Psi (0.5% accuracy). Also the three pressure vessels can be added to a maximum confining pressure and upstream pore pressure of 10,000 psi (0.5% accuracy) independently. Downstream pore pressures are also controlled by one syringe pump and differential pressure transducers (Maximum 500 psi with 0.5% accuracy) are used to sense the pressure difference between upstream and downstream. These pumps can also create a constant flow with the flow rate range from $0.5 \times 10^{-6}\ m^3/s$ to $1.67 \times 10^{-13}\ m^3/min$. Because the syringe pumps work as a fluid container, they can be used to measure the compressive storage of the samples porosity and the upstream and downstream reservoir.

Temperature fluctuation is very critical for the pressure change according to the ideal gas law. In order to maintain a constant temperature, all the pressure vessels, valves and transducers are placed in the oven. The fluctuation of temperature is kept to $\pm 0.1\ ^oC$ and the absolute fluctuation of temperature over 48 hours in the oven is less than $0.2\ ^oC$. All the pumps are placed outside of the oven and covered with

insulation to reduce the fluctuation of temperature.

The whole system is controlled and monitored by computer interface, where the confining, upstream, differential pressure and temperature are recorded against time. In this study, we measure the gas permeability of shale core plugs. The gas we used in the experiment is nitrogen. As is known, methane is the main component of natural gas in shale. However, methane is unstable and it is unsafe to be used directly in the experiment. Nitrogen is an inert gas with the kinetic molecular diameter of 0.364 nm, which is similar to the kinetic molecular diameter of methane gas 0.38 nm. In addition, as an inert gas nitrogen will not react with the organic matter and other compositions of shale samples. So nitrogen is an optimum fluid to simulate the in-situ condition of gas transportation.

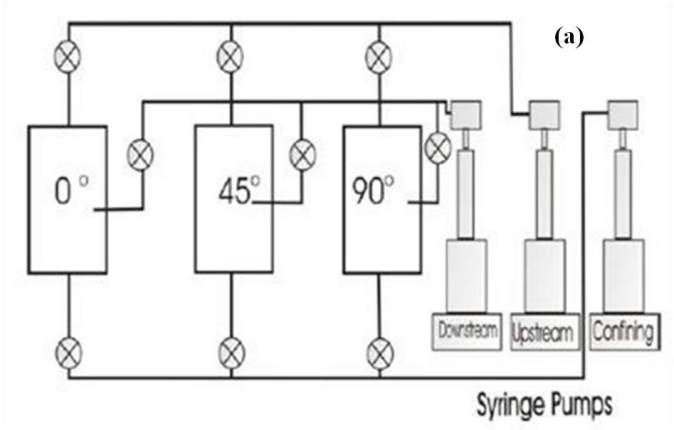

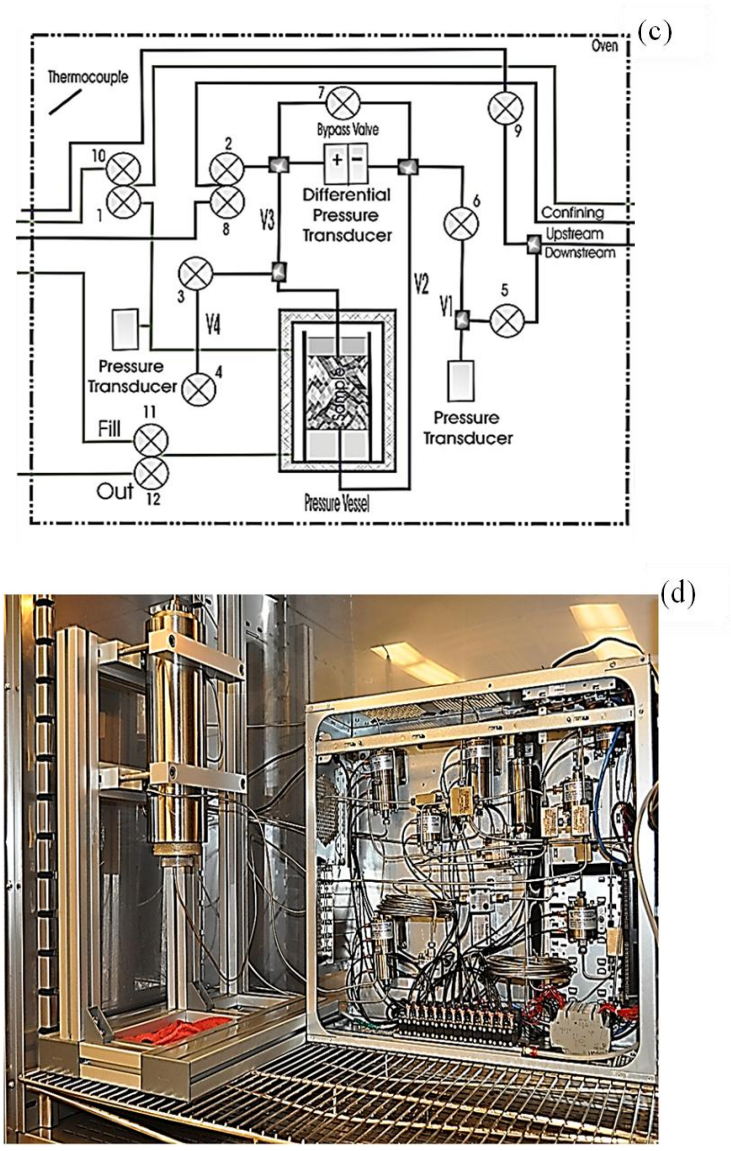

Figure 3-6: a) Schematic diagram of the whole permeability measurement system, b) Photo of the measurement system, c) Schematic diagram of one pressure system, d) Photo of one pressure system in the oven (*after Metwally and Chesnokov, 2010*).

3.5 Porosity and other parameter measurement

3.5.1 Compressibility β_f and compressibility factor Z

According to equation 3-23, the compressibility of the fluid is needed to calculate the permeability. The storage capacity of reservoir for any fluids depends not only on fluid compressibility but also on the compressibility of reservoir materials. So the fluid compressibility can be measured experimentally as follows:

$$\beta_f = \frac{\delta V/\delta P}{V_0} \tag{3-24}$$

where β_f is the fluid compressibility (MPa^{-1}), V_0 is the initial pump volume, δV is the volume change and δP is the relative pressure change. The β_f can be calculated based on the syringe pump volume V_0. Then, by applying the same procedure to make δV and δP for fluid in reservoir, together with β_f, reservoir volumes can be determined. In our experiment, they also can be directly measured by calculating the change in syringe pump volume δV during the filling stage under the constant pressure mode, which means the δP in the pump will be zero. This current approach can measure the storage capacity of the experiment reservoirs at any pressure up to 10,000 psi with an accuracy of 0.01×10^{-9} m^3.

In our experiment, we use nitrogen gas as fluid. As is known, the compressibility of gas β_g is much greater than the reservoir material compressibility; so the reservoir material compressibility can be reasonably neglected and the

following equation can be used to calculate the gas compressibility,

$$\beta_g = \frac{P_m - Z}{P_m(1-P_m)} \qquad (3\text{-}25)$$

where Pm is the mean pore pressure (MPa), and z is the compressibility factor of fluid. Compressibility factor of nitrogen gas can be calculated by using SUPERTRAPP™ software (Figure 3-8), which is an interactive computer program for predicting thermodynamic and transport properties of pure fluids and fluid mixtures. Compressibility factor of nitrogen changes with pressure at temperature of 25 °C has been shown in figure 3-7.

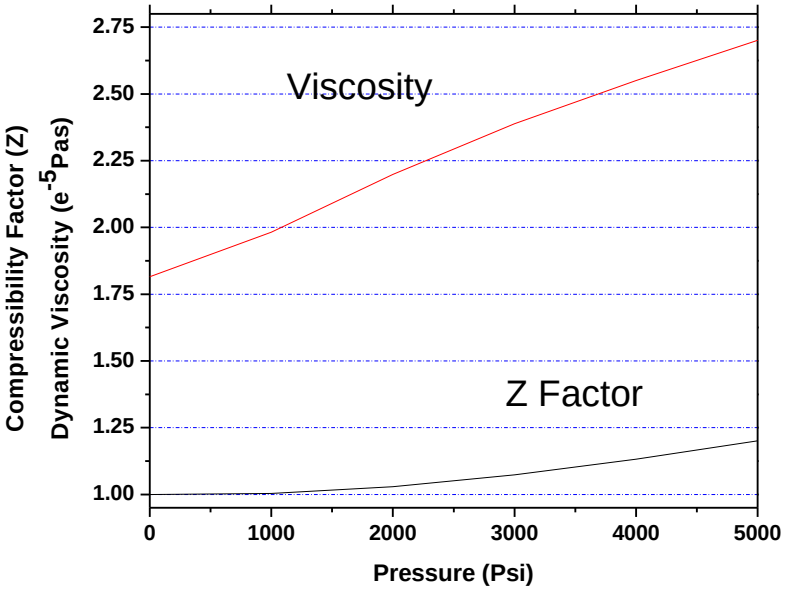

Figure 3-7: The compressibility factor (Z) and dynamic viscosity of nitrogen gas against pressure at temperature of 25 °C. Parameters come from SUPPERTRAPP™ software.

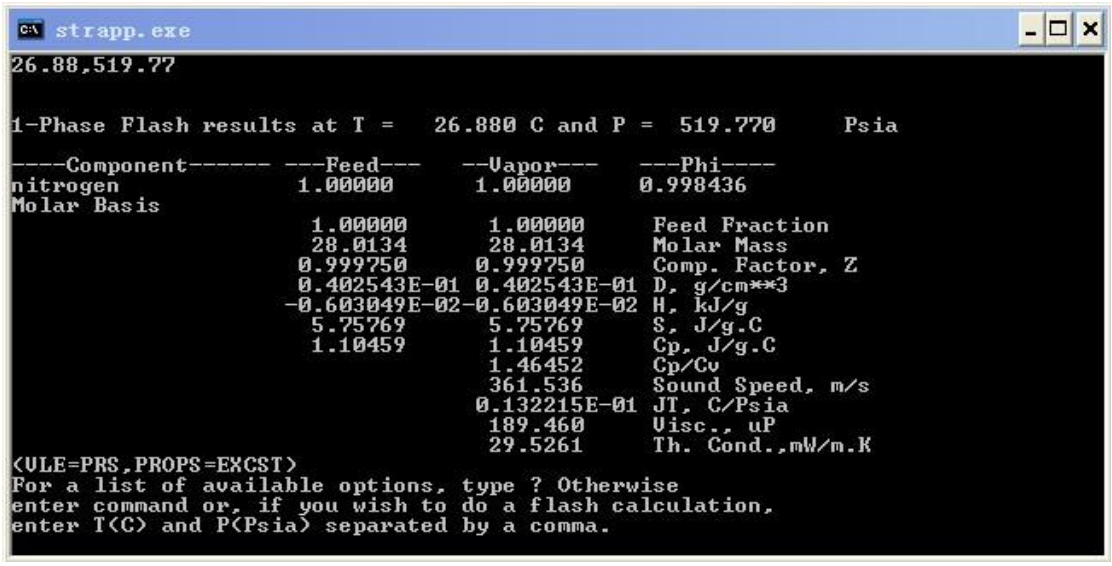

Fig 3-8: Interface of SUPERTRAPPTM software, which is used to determine the Z factor and dynamic viscosity of nitrogen in this study.

3.5.2 Effective porosity ($\emptyset_e$)

Porosity of rock can be defined as the fraction of pore volume or void space within bulk volume. It is the non-solid portion of the rock filled with fluids and is mathematically given as:

$$\emptyset = \frac{V_P}{V_B} = \frac{V_B - V_G}{V_B} \tag{3-26}$$

Where V_P is the pore volume of the rock sample, V_B is the bulk volume of the sample, and V_G is the grain volume of the sample. $\emptyset$ is the porosity of shale sample. Sediments are porous medium and pores are occupied by fluid like natural gas, oil, and water.

Effective porosity is defined as the ratio of the interconnected pore volume in a rock to the bulk volume, which contributes to fluid flow in a rock or reservoir. Effective porosity excludes isolated pores and pore volume occupied by water

adsorbed on clay minerals or other grains (Oilfield Glossary). While total porosity is defined as the ratio of total void space in a rock to the bulk volume, which includes all void space regardless of whether the pores are interconnected or isolated. Total porosity can be measured by using the crushed sample.

In this study, effective porosity is measured under the same confining pressure and temperature conditions as the permeability measurement. We use nitrogen as fluid to measure the effective porosity. During the experiment, nitrogen is used to saturate the shale sample under a constant confining pressure. The gas of nitrogen was firstly stored in a known volume reservoir V_1 with an equilibrium pressure of P_1 (schematic picture in Figure 3-6(c)). Then it is released into the downstream reservoirs with known volume of V_2 and V_3 (schematic picture in Figure 3-6(c)) and the pore volume Vp of the shale sample. When the system reaches to equilibrium again, we can get a new pressure of P_2 (see Figure 3-9).

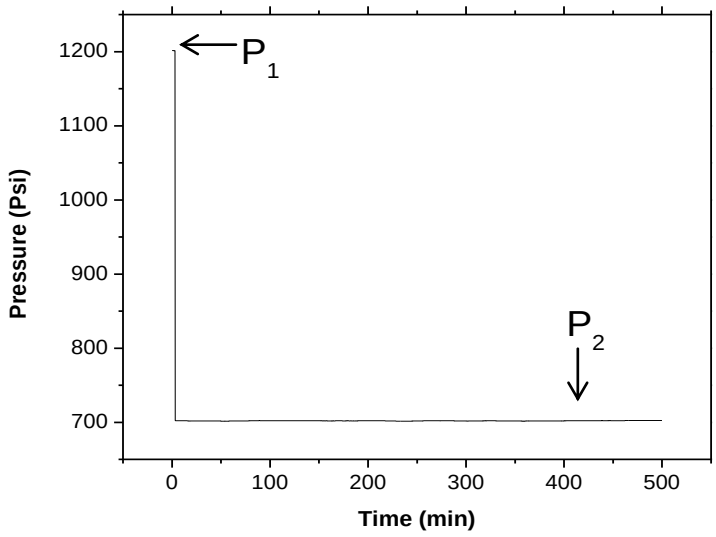

Figure 3-9: Pressure reading against time during the porosity measurement. Samples are saturated with nitrogen gas.

Using the Boyle's law, the pore volume Vp can be calculated from the following equation:

$$z_2 P_1 V_1 = z_1 P_2 (V_1 + V_2 + V_3 + V_p) \quad (3\text{-}27)$$

where Z_1 is the compressibility factor of fluid at equilibrium pressure P_1 and Z_2 is the compressibility factor of fluid at equilibrium pressure P_2.

The pore pressure of this experimental system was designed to have a maximum value up to 5,000 Psi. The pore volume calculation will be very sensitive to the pressure reading and thus sensitive to the temperature. Our whole pressure system is kept in an oven to make temperature stable. As the core plugs have regular geometric shape, the sample bulk volume V_b can be calculated from the direct measurement of diameter and length of the sample. Then, the effective porosity can be calculated as follows:

$$\emptyset_e = \frac{V_p}{V_b} \quad (3\text{-}28)$$

3.5.3 Viscosity

Viscosity is the quantity that describes a fluid's resistance to flow. According to equation 3-23, the viscosity of nitrogen gas is needed in order to calculate gas permeability. As is known, the viscosity of water at a constant temperature is usually constant (1×10^{-3} Pa·s), which means it is independent of pressure except at very high pressure. On the other hand, the gas viscosity is strongly dependent on pressure.

Viscosity of nitrogen gas can be calculated by using SUPERTRAPP^{TM} software, which is an interactive computer program for predicting thermodynamic and transport properties of pure fluids and fluid mixtures. Viscosity of nitrogen changes with pressure at temperature of 25 ^{o}C has been shown in Figure 3-7.

3.6 Sample preparation

Four-inch Barnett Shale cores were drilled from wells and shipped to our lab. The original cores were covered by wax to prevent drying. In order to measure permeability tensor and elastic wave properties, cylindrical core plugs (1 inch × 2 inch) were cut from carefully selected regions of the core samples by using one inch diamond bit and gasoline as a cooling fluid. Three core plugs were cut from one core sample in the direction of parallel, perpendicular and at 45^{o} angles to the axis of symmetry (assuming that shale has transversely isotropic symmetry and bedding plane is the plane of symmetry). The two ends of a core plug were polished parallel to each other within 0.05 mm, an important step which helps ensure that the ultrasonic velocity is accurately measured and the pressure can be evenly applied on both ends of the sample.

The core plugs are cleaned in Soxhlet extraction apparatus (Figure 3-10(a)) with boiling toluene to remove the drilling fluid contaminants. Then we heat samples in a vacuum oven (Figure 3-10(b)) at 100 ^{o}C for 5-8 hours to remove free water. The vacuum level is about 0.08 MPa. After that, the plugs are removed from the oven and

allowed to cool for at least 30 min in a desiccator (Figure 3-10(c)) before any experiment is run. The weight of the plugs is measured by using a digital balance and the bulk volume is calculated from their dimensions.

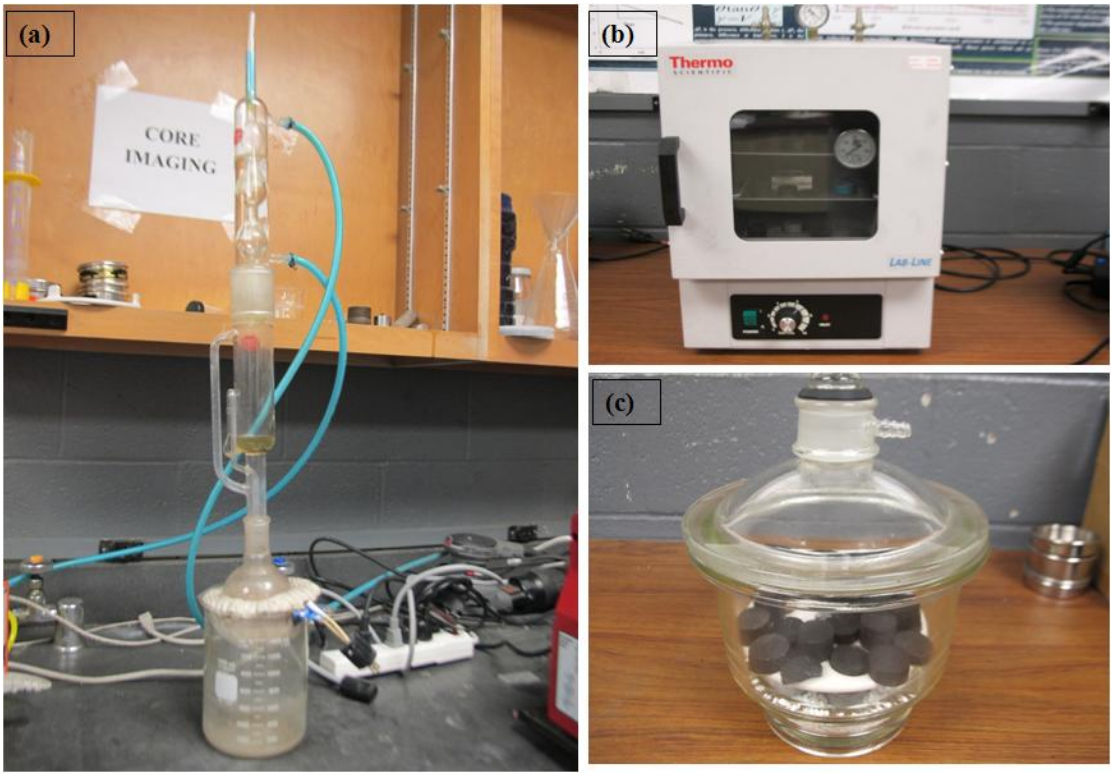

Figure 3-10: a) Soxhlet extraction apparatus for cleaning core plug, b) Vacuum oven for drying and removing free water, c) Desiccator for keeping core plugs as dry sample.

3.7 Uncertainty of gas permeability measurement

In current technique, transport of gas through the rock matrix is depicted as Darcy's flow. Therefore, the error bar of gas permeability can be quantified by using the Darcy's law, which can be presented as,

$$k = -\frac{Q\mu L}{A(P_u - P_d)} \tag{3-29}$$

Where A is cross section of core plug (m^2) and Q is total discharge (m^3/s). So the error bar of permeability Δk can be derived as,

$$\frac{\Delta k}{k} = \sqrt{\left(\frac{\Delta Q}{Q}\right)^2 + \left(\frac{\Delta L}{L}\right)^2 + \left(\frac{\Delta \mu}{\mu}\right)^2 + \left(\frac{\Delta A}{A}\right)^2 + \left(\frac{\Delta P_u}{P_u}\right)^2 + \left(\frac{\Delta P_D}{P_D}\right)^2} \tag{3-30}$$

There are several errors that can come from different sources in the measurement. The permeability calculation for gas shale is very sensitive to changes of differential pressure. The error related to differential pressure is minimized by using digital transducers to read the pressure difference across the sample and keeping upstream pressure constant (± 1 psi) by syringe pump. Because confining pressure has a substantial effect on the measurement of permeability and porosity, it is also controlled by reducing fluctuation in confining pressure to within ± 1 psi by using syringe pump. Temperature also plays an important role in the pressure change. The error associated with temperature fluctuation is minimized by controlling temperature to ± 1 ^{o}C in the specially designed oven.

The error associated with the gas adsorption effect, which may underestimate permeability when gas permeability is measured (Bustin et al. 2008), can be neglected

because we used nitrogen gas, which is inert and the storage capacity of upstream reservoir in the current technique is infinite.

There is a systematic error associated with shale's heterogeneity because we assume the pressure gradient is constant along the core plug. According to Trimmer (1981), this error is a function of the ratio of the effective sample pore volume to the reservoir volumes. It can be minimized to less than 1% by adjusting the ratios of the sample pore volume to downstream reservoir volume to be less than 0.1.

Neglecting other errors, the uncertainty of permeability measurements by using the current technique outlined above is estimated to be less than 3%.

Chapter 4 Results and Analysis

4.1 Ultrasonic velocity

4.1.1 Velocity and elastic properties

We use the three plug technique described in Chapter 2 to measure the ultrasonic velocity of shale samples under room condition. As shale samples with bedding plane are assumed to be a VTI medium, the two S-waves, Vs_1 and Vs_2 passing through the vertical sample should have the same value. The P-wave velocity passing through the horizontal sample should be greater than that passing through the vertical sample. We observed these phenomena for all 12 samples, as shown in below Figure 4-1 and Figure 4-2. There are two samples that are shown to be isotropic material. Sample B (Figure 4-2) and sample I, which have the same P-wave and S-wave in all directions. No bedding planes can be seen or detected on these two samples using normal un-enhanced visualization techniques (microscopes) (both of them are too tight to be detected for any permeability by current technique, refer to Chapter 4.2). Except for the two isotropic samples, the other ten samples are shown to have anisotropic properties. Velocity results are summarized in the Table 4-1.

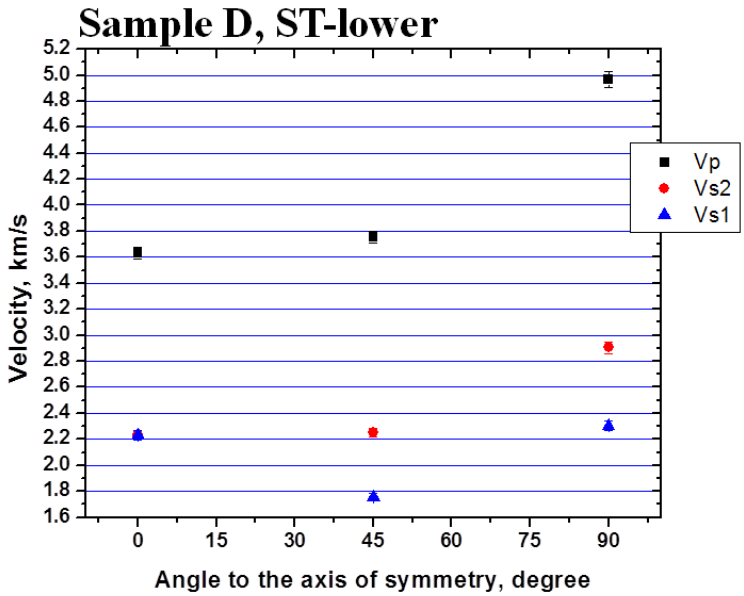

Figure 4-1: Anisotropic sample with transversely isotropic property shows two equal shear waves through vertical direction, shear wave splitting at other directions and P-wave variations

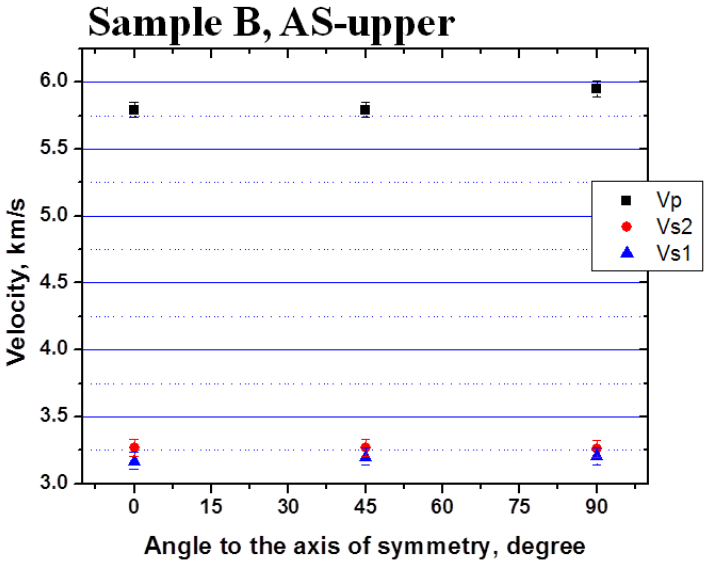

Figure 4-2: Isotropic sample which shows almost the same Vp, Vs1, and Vs2 at all directions. No shear wave splitting at 45 degree and parallel to bedding plane

The five elastic constants (C11, C33, C44, C66, C13) were calculated from wave velocities (Vp, Vs1, Vs2), shown in Table 4-2. The Thomsen parameters, P-wave anisotropy ε, S-wave anisotropy γ, and factor δ were calculated.

Table 4-1: Measurement results of ultrasonic velocity and density based on three plug techniques. The error bar for Vp is 1% and for Vs is 2%

	Degree	**Length**	**Density**	**Vp**	**Vs1**	**Vs2**
Sample		*inch*	*g/cm3*	*km/s*	*km/s*	*km/s*
A-1	90^o	**1.663**	**2.522**	**4.923**	**2.352**	**2.983**
A-2	0^o	**0.406**	**2.548**	**3.130**	**2.236**	**2.255**
A-3	45^o	**0.204**	**2.535**	**4.056**	**2.012**	**2.449**
B-1	90^o	**0.942**	**2.662**	**5.952**	**3.207**	**3.260**
B-2	0^o	**0.734**	**2.670**	**5.793**	**3.170**	**3.192**
B-3	45^o	**0.479**	**2.665**	**5.794**	**3.202**	**3.271**
C-1	90^o	**0.633**	**2.404**	**4.701**	**2.227**	**2.861**
C-2	0^o	**0.393**	**2.407**	**3.015**	**2.126**	**2.144**
C-3	45^o	**0.259**	**2.399**	**3.257**	**2.223**	**2.300**
D-1	90^o	**0.954**	**2.475**	**4.965**	**2.303**	**2.905**
D-2	0^o	**0.216**	**2.471**	**3.630**	**2.230**	**2.230**
D-3	45^o	**0.390**	**2.566**	**3.752**	**1.756**	**2.251**
E-1	90^o	**0.794**	**2.559**	**4.690**	**2.305**	**2.949**
E-2	0^o	**0.536**	**2.716**	**4.477**	**2.793**	**2.815**
E-3	45^o	**0.252**	**2.714**	**5.238**	**3.018**	**3.362**
F-1	90^o	**1.045**	**2.866**	**4.897**	**2.853**	**3.047**
F-2	0^o	**0.233**	**2.626**	**3.565**	**2.368**	**2.368**
F-3	45^o	**1.213**	**2.747**	**5.102**	**2.941**	**3.090**
G-1	90^o	**0.915**	**2.490**	**4.469**	**2.083**	**2.905**
G-2	0^o	**0.306**	**2.499**	**2.944**	**2.313**	**2.313**
G-3	45^o	**0.355**	**2.545**	**3.665**	**2.437**	**2.732**
H-1	90^o	**0.712**	**2.607**	**4.734**	**2.249**	**3.014**
H-2	0^o	**0.209**	**2.461**	**3.160**	**2.176**	**2.176**
H-3	45^o	**0.422**	**2.625**	**4.060**	**1.798**	**2.094**
I-1	90^o	**0.567**	**2.675**	**4.338**	**2.466**	**2.483**
I-2	0^o	**0.287**	**2.637**	**4.238**	**2.497**	**2.497**
I-3	45^o	**0.268**	**2.613**	**4.420**	**2.484**	**2.521**
J-1	90^o	**0.803**	**2.530**	**4.928**	**2.589**	**3.149**
J-2	0^o	**0.186**	**2.529**	**3.810**	**2.313**	**2.313**
J-3	45^o	**0.230**	**2.529**	**4.005**	**1.698**	**2.070**
K-1	90^o	**0.889**	**2.399**	**4.784**	**2.407**	**3.027**
K-2	0^o	**0.353**	**2.449**	**3.053**	**2.308**	**2.320**
K-3	45^o	**0.558**	**2.446**	**4.788**	**2.402**	**3.055**
L-1	90^o	**1.252**	**2.666**	**5.301**	**2.810**	**3.125**
L-2	0^o	**0.377**	**2.735**	**3.787**	**2.520**	**2.533**
L-3	45^o	**0.134**	**2.700**	**4.613**	**2.438**	**2.474**

Table 4-2: Elastic constant calculated from P-wave and S-wave

	Density	**C11**	**C44**	**C66**	**C33**	**C13**	ε	γ	δ
Sample	*g/cm3*	*Gpa*	*Gpa*	*Gpa*	*Gpa*	*Gpa*			
A	**2.54**	**61.44**	**14.02**	**22.56**	**24.84**	**4.79**	**0.74**	**0.30**	**0.06**
B	**2.67**	**94.43**	**27.42**	**28.32**	**89.45**	**32.11**	**0.03**	**0.02**	**-0.06**
C	**2.40**	**53.11**	**11.92**	**19.67**	**21.85**	*	**0.72**	**0.33**	*
D	**2.50**	**61.74**	**13.28**	**21.14**	**33.00**	*	**0.44**	**0.30**	*
E	**2.66**	**58.58**	**14.15**	**23.16**	**53.37**	**61.82**	**0.05**	**0.32**	**1.45**
F	**2.75**	**65.86**	**22.35**	**25.49**	**34.90**	**46.15**	**0.44**	**0.07**	**3.56**
G	**2.51**	**50.17**	**10.89**	**21.20**	**21.77**	**4.07**	**0.65**	**0.47**	**-0.10**
H	**2.56**	**57.48**	**12.97**	**23.30**	**25.60**	**12.48**	**0.62**	**0.40**	**0.44**
I	**2.64**	**49.71**	**16.07**	**16.29**	**47.45**	**22.50**	**0.02**	**0.01**	**0.21**
J	**2.53**	**61.44**	**16.96**	**25.08**	**36.72**	**-8.28**	**0.34**	**0.24**	**-0.41**
K	**2.43**	**55.64**	**14.09**	**22.28**	**22.66**	**41.77**	**0.73**	**0.29**	**5.66**
L	**2.70**	**75.90**	**21.32**	**26.37**	**38.73**	**9.87**	**0.48**	**0.12**	**0.23**

The sign * represents the failure to calculate C13 due to the heterogeneity of shale sample.

The density in Table 4-2 is the average value of densities of three plugs in Table 4-1. As we know, density is a parameter which reflects the mineral composition, TOC, and porosity of rocks. It is ideal to get the densities of all three core plugs that are the same in order to stand for the same material. Spatial heterogeneity will cause the deviation of densities and elastic properties even though three samples are cut from the adjacent area, which is also one of the weaknesses of the three plug technique. The main reason for two samples failing to be appropriate for calculating C13 is due to the high heterogeneity of the core sample.

4.1.2 Seismic anisotropy of shale

Anisotropy values ranges from 5% to 73% (excluding the two isotropic samples) for P-wave parameter ε and 7% to 47% for S-wave parameter γ. Several samples show a very high anisotropy. We cross plot the anisotropy parameters ε and γ in Figure 4-3. Only half of samples have a good linear correlation for ε versus γ. The heterogeneity of the samples most probably contributes to the scattering of other samples.

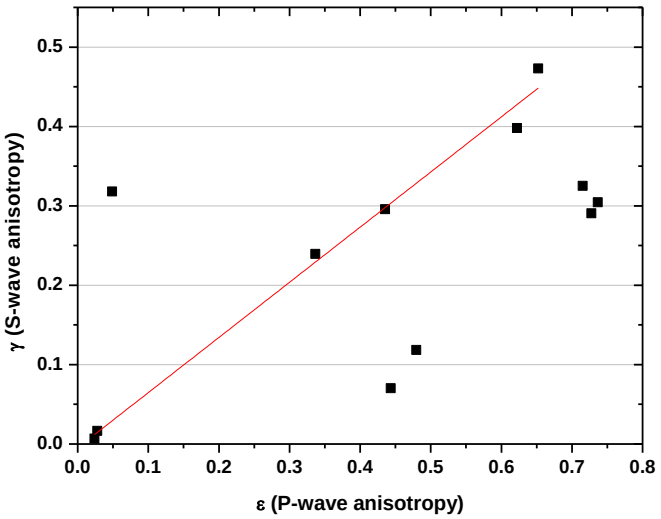

Figure 4-3: Relationship between P-wave anisotropy parameter ε and S-wave anisotropic parameter γ for shale sample

The coefficient δ has also been plotted against the parameter ε in Figure 4-4. As the calculation of δ involves variations of both P-wave and S-wave, the uncorrelated curve is understandable.

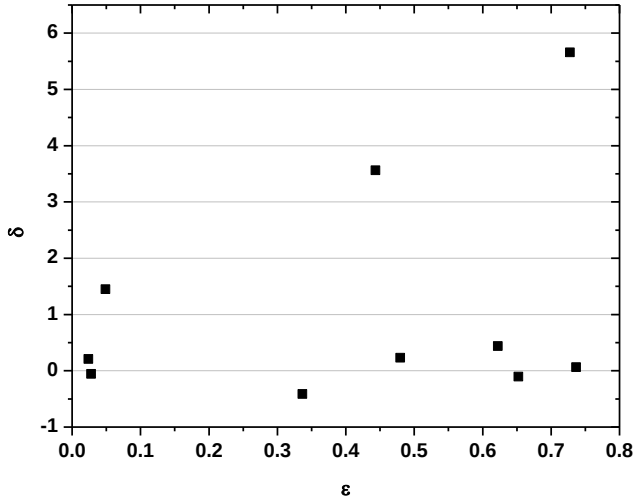

Figure 4-4: Relationship between anisotropy parameter ε and δ for shale sample. No apparent correlation can be observed.

4.1.3 TOC and mineralogy effect on velocities

Table 4-3 shows the total organic content (TOC) and mineral composition for the 12 sample sets. TOC is provided by Di Chen from her 2012 Master's thesis "Modeling Elastic Properties of Gas Shale and Microstructure Study on Barnett Shale". Mineral composition data is provided by Dr. Yasser Metwally, using X-ray Diffraction.

Although the majority of the minerals found were quartz, carbonates, and clays, different set of samples vary in mineral concentration. Both of the two isotropic samples have very low percentage of TOC. We cross plot the TOC and mineral composition with velocity and anisotropy factors. Only TOC shows some correlative relationships with P- and S-wave velocities and anisotropy parameters.

Table 4-3: TOC and mineralogy for all samples.

	TOC	**Mineralogy (wt%)**				
Sample	*wt %*	*Quartz*	*Carbonate*	*Clay*	*Sulfates & Halites*	*others*
A	**5.13**	**57**	**12**	**18**	**5**	**8**
B	**0.80**	**7**	**62**	**7**	**22**	**2**
C	**5.93**	**60**	**13**	**15**	**5**	**7**
D	**5.80**	**36**	**31**	**12**	**13**	**8**
E	**2.87**	**47**	**20**	**21**	**7**	**5**
F	**2.54**	**66**	**7**	**21**	**2**	**4**
G	**2.84**	**66**	**5**	**20**	**4**	**5**
H	**3.48**	**52**	**13**	**21**	**6**	**8**
I	**0.12**	**71**	**4**	**16**	**1**	**8**
J	**3.60**	**24**	**15**	**44**	**10**	**7**
K	**4.76**	**71**	**4**	**18**	**2**	**5**
L	**3.91**	**71**	**7**	**16**	**1**	**5**

Except for two isotropic samples have very low TOC (less than 1%), the TOC for other Barnett Shale samples is 2.5%-5.9%. From below Figure 4-5 (a) and (b), a dependence of velocity and density on organic content is observed. In general, P- and S-wave velocities decrease with the increase of organic content. Density also decreases with the increase of organic content, as shown in Figure 4-5 (c). Similar dependence of shale velocity and density on TOC was observed by Vernik and Liu (1997).

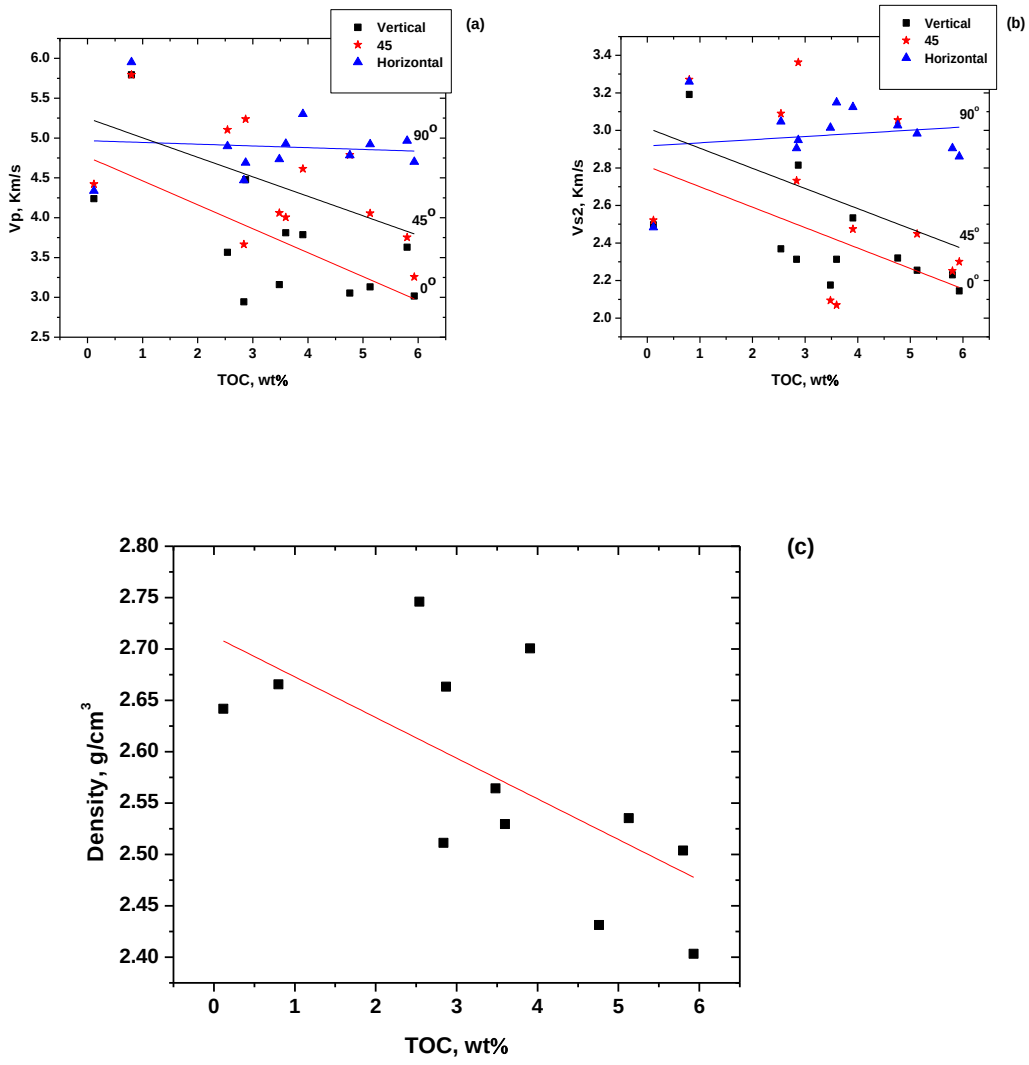

Figure 4-5: (a) P-wave velocities against TOC for all vertical, 45 degree, and horizontal shale plugs. (b) S-wave velocities against TOC for all vertical, 45 degree, and horizontal shale plugs. (c) Density against TOC.

Anisotropy of wave velocity is observed to have dependent on TOC also. Both P-wave parameter ε and S-wave parameter γ increase with the increase of organic content. Similar dependence of anisotropic parameters on TOC was observed in the past (Sondergeld et al., 2000).

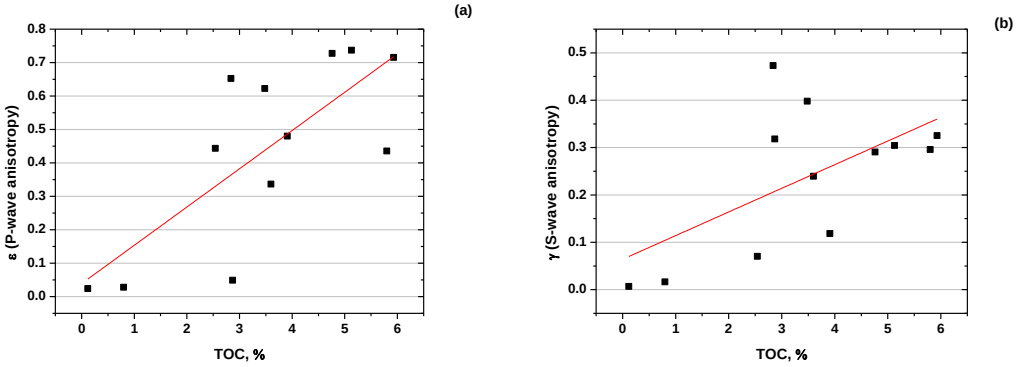

Figure 4-6: Plot of ε (P-wave anisotropy) and γ (S-wave anisotropy) against TOC.

4.1.4 Velocity measured after permeability measurement

In order to better understand if there were any changes in the elastic properties that happened during the permeability experiment with the changes of confining pressure and pore pressure, we measured the velocity again after the permeability measurement. Several measurements were made with different time intervals to see is any changes could be detected with time.

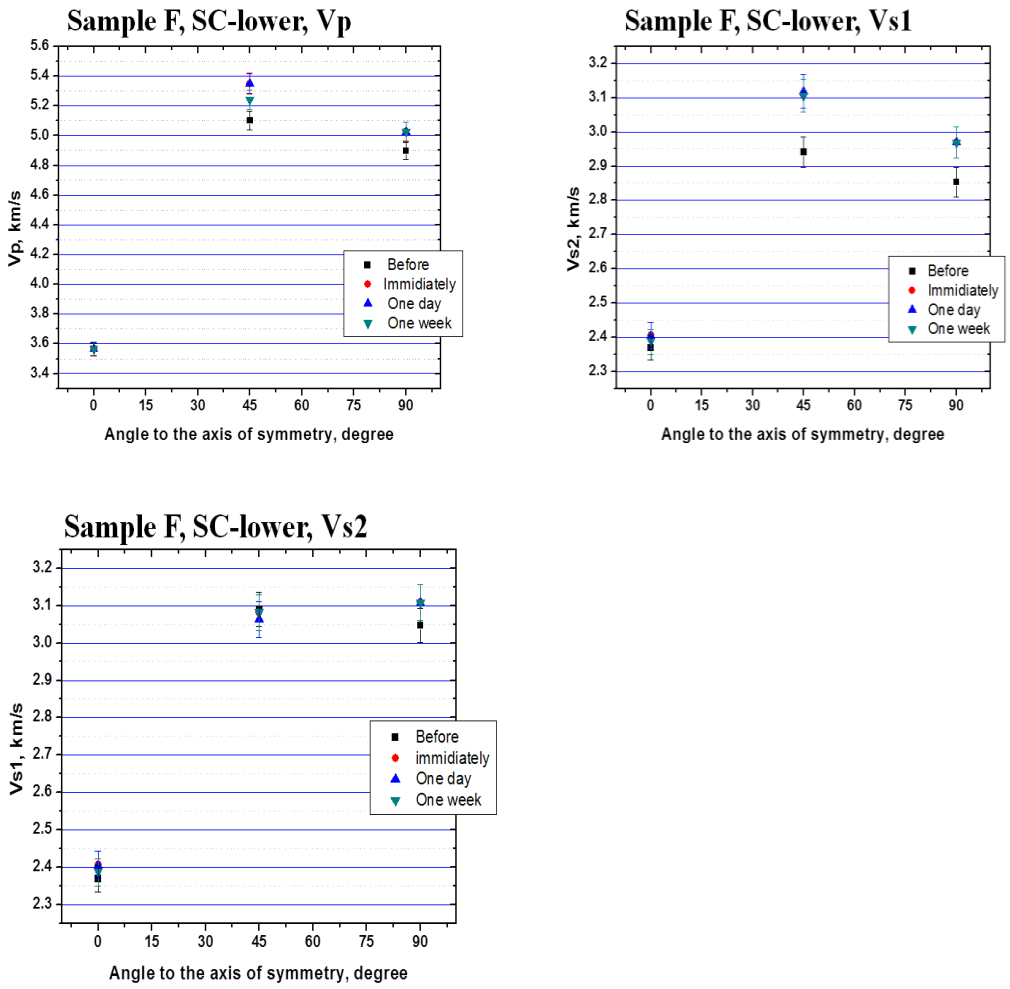

Figure 4-7: Velocity comparison of the before permeability measurement with after permeability measurements (velocity measured immediately, one day, and one week after permeability experiment).

No big fluctuations of P-wave and the faster shear wave velocities were observed, as shown in the Figure 4-7. Only the slower shear waves have a small increase (less than 5%) in the direction of 45 degree and parallel to bedding plane. The results are reasonable as the fluid used in the permeability measurement is nitrogen, which is an inert gas which will not react with the Total Organic Carbon content and other compositional components of the core samples. The confining and

pore pressures added on the core plugs during permeability measurement are around or less than in-situ pressures, so the internal structural character of the samples stay the same when pressures are released. On the other side, shale is very fragile and the core plugs break easily along the bedding plane. Three samples have been broken during the permeability measurement.

4.2 Permeability

We designed two scenarios to measure the gas permeability in our lab. The first procedure is changing the confining pressure (pressure points were 1000psi, 2000psi, 3000psi, 4000psi, and 5000psi) under a constant pore pressure (500psi) to investigate the behaviours of permeability and other storage parameters. Six samples were experimented with by using this procedure. It usually takes approximately 2 weeks to measure the permeability (porosities under different confining pressures measured simultaneously) of one set of samples just in one confining pressure condition because of the very small permeability (micro or nano scale) in the vertical direction. In order to expedite the experiments, we also employed another procedure to measure the gas permeability for another six samples by simulating the in-situ condition (confining pressure 4000psi and pore pressure 2000psi). The results are listed in Table 4-4 (3 broken samples, 2 very tight samples have no responses to pressure change, and 3 samples are still in the process of being measured. Those samples are and their progresses are excluded from the results presented in this thesis).

Table 4-4: Measured gas permeability and porosities in three directions with different confining pressure. Ar is the anisotropy ratio of permeability.

Confining pressure (pore pressure 500psi)		**1000psi**		**2000psi**		**3000psi**		**4000psi**		**5000psi**	
		Porosity	**Permeability**	**Porosity**	**Permeability**	**Porosity**	**Permeability**	**Porosity**	**Permeability**	**Porosity**	**Permeability**
Core	**Direction**		*uDarcy*		*uDarcy*		*uDarcy*		*uDarcy*		*uDarcy*
D2	0^o (k_{zz})	0.032	0.010	0.014	0.007	0.006	0.005	0.004	0.005	0.001	0.004
D3	45^o (k_{xz})	0.076	787.05	0.068	141.09	0.058	54.32	0.057	22.26	0.058	6.86
D1	90^o(k_{xx})	0.082	3,530.82	0.053	722.59	0.048	463.95	0.045	255.56	0.044	110.26
	Ar (ratio)		3E-06		1E-05		1E-05		2E-05		4E-05
E2	0^o (k_{zz})	0.016	0.475	0.009	*	*	*	*	*	*	*
E3	45^o (k_{xz})	0.062	*	*	*	*	*	*	*	*	*
E1	90^o(k_{xx})	0.076	2,434.14	0.058	472.82	0.057	141.38	0.047	47.67	*	*
	Ar (ratio)		2E-04		*		*		*		*
G2	0^o (k_{zz})	0.019	0.125	0.017	0.056	0.006	0.26	0.005	*	0.004	0.047
G3	45^o (k_{xz})	0.082	43.79	0.013	5.16	0.013	2.78	0.010	1.37	0.002	0.56
G1	90^o(k_{xx})	0.061	17,542.35	0.015	10,900.26	0.005	6,583.52	0.003	3,936.38	0.001	2,350.27
	Ar (ratio)		7E-06		5E-06		4E-05				2E-05
K2	0^o (k_{zz})	0.005	0.009	0.004	0.007	0.003	0.005	0.002	0.005	0.001	0.003
K3	45^o (k_{xz})	0.114	64.41	0.109	63.54	0.105	38.78	0.102	24.56	0.098	14.36
K1	90^o(k_{xx})	0.087	250.45	0.081	200.11	0.079	120.78	0.077	89.75	0.077	76.23
	Ar (ratio)		4E-05		4E-05		4E-05		5E-05		4E-05

The symbol * represents missing or invalid raw data used to calculate permeability due to obscure or no responses to pressure change of core plugs.

4.2.1 Permeability anisotropy of shale

Table 4-4 shows the measurement results of gas permeabilities for different shale samples. Kzz is the permeability normal to the bedding plane, Kxz is permeability 45^o to bedding plane and Kxx is permeability parallel to bedding plane. The samples display strong anisotropy behaviour at different confining pressure. Permeability normal to bedding plane is demonstrably smaller than the permeability parallel to bedding plane by several orders (Figure 4-8). We use a parameter called anisotropy ratio, A_r, to characterize the anisotropy. It is the ratio of the vertical permeability, Kzz, to horizontal permeability, Kxx, ($A_r = K_{zz}/ K_{xx}$). The anisotropy ratio stays almost the same magnitude when the confining pressures increase (pore pressure constant at 500psi), while the magnitudes of permeability decease by almost two orders. The alignment of minerals, grains, and pores or cracks along a preferential direction at a finer scale than the measurement scale is one of the main sources of anisotropy (Schoenberg, 1994; Georgei et al., 2002; Kwon et al., 2004, Wright et al., 2006; Metwally et al., 2011).

With the assumption of VTI medium, the permeability at any angle to bedding plane can be theoretically derived from permeability normal to the bedding plane Kzz and permeability parallel to bedding plane Kxx. The solid line in Figure 4-8 is the calculated permeability by using Kzz and Kxx. The difference between the measured and theoretical permeability at 45^o could be explained by the uncertainty of the exact orientation of bedding for the 45^o core plug, which is a shortcoming of the three plug

technique. The heterogeneity of shale is another possible reason that could be a likely cause of the difference between the calculated value and the measured value.

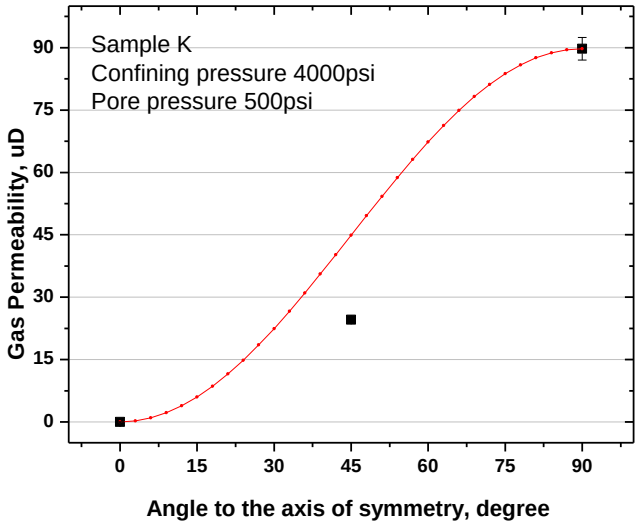

Figure 4-8: Gas permeability measured for three different directions of sample K with confining pressure of 4000Psi and pore pressure 500Psi.

4.2.2 Relationship of confining pressure (constant pore pressure) to permeability and porosity

Permeabilities at all directions decrease nonlinearly with increasing confining pressure or effective pressure (as pore pressure is constant). The rate of decrease is quite different from sample to sample and in different directions, Figure 4-9 shows the decreasing trend for permeability parallel to bedding plane. Effective porosity also has a nonlinear reduction behaviour with the increase of confining pressure. This decrease both on permeability and porosity may be due to the closing of some small pores and/or cracks as effective pressure increases. It can be explained by the flow through micro-cracks model (Metwally et al., 2011).

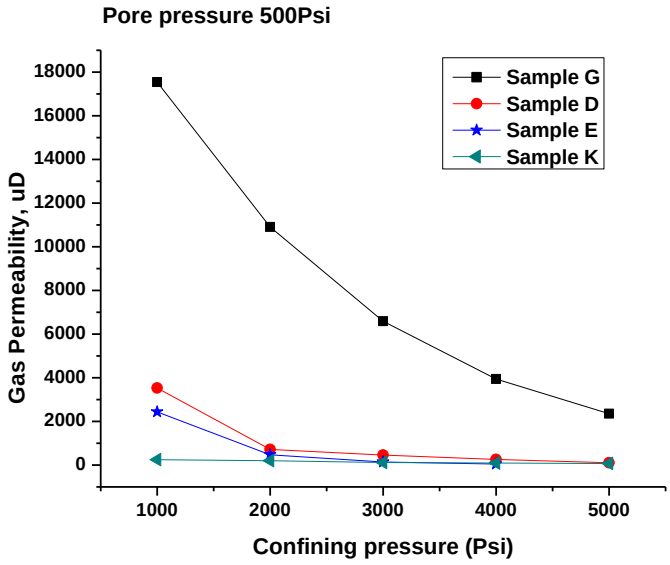

Figure 4-9: Gas permeability parallel to bedding plane decreases with the confining pressure increasing (pore pressure keep as constants of 500Psi)

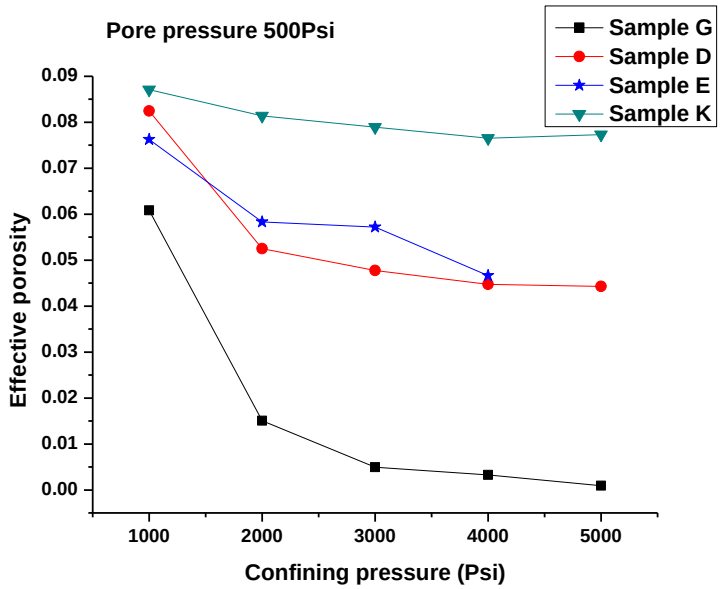

Figure 4-10: Relationship between effective porosity and confining pressure (pore pressure keep as constants of 500Psi)

Comparing Figure 4-9 and Figure 4-10, the effective porosity decreases as permeability decreases, although it does not have a proportional relationship with permeability. Instead, the higher permeability usually bears a relative low porosity in

this case, which indicates that the connected pore volume is not the only factor that will affect the flow mechanism in the rock matrix.

4.2.3 Relationship between elastic constant and permeability

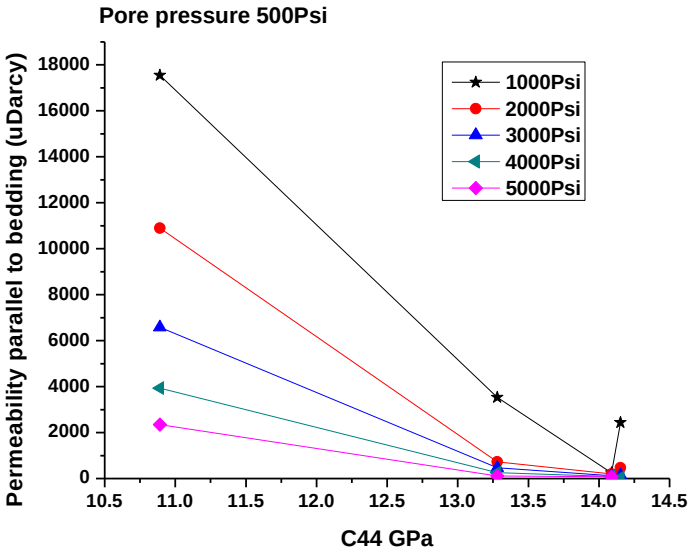

Figure 4-11: Relationship between permeability parallel to bedding plane and elastic constant C44.

In order to find the relationship between elastic properties and gas transportation capability, we cross plot all the five elastic constants with gas permeability. Except for C44, no correlation has been found for other elastic constants. As shown in Figure 4-11, we can see a clear decreasing trend of permeability parallel to bedding plane with the increasing of C44, although there are some deviations at low confining pressure condition. C44 is derived from $V_{sv,90}$, which is the shear velocities polarized normal to the bedding plane. So, it is important to recognize that this phenomena may reveal that the SV wave may reflect or be a way to characterize those features of

connectivity and channel micro-structure between the bedding planes, which acts as a controls on fluid flow through those channels.

Because C44 is determined by using the horizontal plug, the same plug we used to get the permeability parallel to bedding plane, uncertainties from heterogeneity of shale and density variation between three plugs are minimized. Therefore, based on our measurement and data analysis, we think that C44 or $V_{sv,90}$ may be a good indicator for qualitatively estimating permeability. However, statistical studies need to be conducted to validate these observations and before this correlation can be used to predict gas shale permeability in the realm of unconventional gas field development and reservoir characterization

Chapter 5 Summary and Discussion

We investigated the elastic properties and permeability of Barnett Shale samples from the Fort Worth Basin in north Texas, USA. A three plug technique was used to measure ultrasonic velocity at ambient room pressure and temperature conditions. The estimated uncertainty for P-wave measurements is 1% and for S-waves is 2%. Permeability, porosity, and other critical reservoir storage parameters were measured by using a specially designed laboratory apparatus over a range of confining and pore pressures. New transient pressure techniques for measuring the permeability of unconventional rocks, developed by Metwally and Sondergeld (2011), have been employed with success in this study. The estimated uncertainty for the permeability measurements presented in this work is less than 3%. Based on our measurements and data analysis, these results show that,

1. The Barnett shale samples have high anisotropy in both velocity and permeability. On the one hand, P-wave anisotropy parameter ε ranges from 5% to 73% and S-wave parameter γ ranges from 7% to 47%. The high anisotropy value for velocity is reasonable because all velocities we measured are under room condition. Anisotropy parameter ε and γ decrease with increasing effective pressure. Experiments done on shale's velocity anisotropy have revealed this kind of trends. For example, "Under the dry condition, the P-wave anisotropic ε decreases from 0.95 to 0.42 and S-wave anisotropic γ decreases from 0.78 to

0.52, when the effective pressure increases from 10 MPa to 80 MPa" (Deng et al., 2009). As seismic anisotropy can be caused by thin layers, preferential alignment of microcracks and mineral grains (Wang, 2001; Deng et al, 2009), release of confining pressure will develop more microcracks, especially when shale cores are kept in room condition after they were drilled from well. On the other hand, permeability anisotropy ratio A_r is quite large and ranges from 2E-4 to 3E-6. The permeability parallel to the bedding plane is several orders larger than permeability normal to the bedding plane, which means that the gas flow parallel to the bedding plane best characterizes the maximum gas transportation orientation in gas shale matrix.

2. TOC (total organic content) shows control on the velocity, density, and the anisotropy parameters (ε and γ). In general, velocity and density decrease with increasing organic content, which means the seismic reflectivity is affected by the richness of organic content. Meanwhile anisotropy increases with increasing of organic content. The correlation between TOC and anisotropy may indicate that the alignment of organic matter is more likely parallel to bedding plane.
3. Both permeability and effective porosity decreased with the increase of effective pressure. The results are understandable because micro-cracks and pores tend to close and the rock grains have better contact with the increase of effective pressure. The decreasing rates are different for different samples at different directions. There is no proportional relationship between effective porosity and gas permeability, which shows that there are more factors that control the fluid

transportation mechanism instead of connected pore volume

4. The elastic constant C44 shows correlation with the dominant permeability (parallel to bedding plane), which may be a good indicator for estimating permeability in the field. This is because shear wave velocity measurements can be made by various tools and methods used in the modern oilfield setting or on samples derived from wellbore cores and brought into the laboratory for detailed measurements. Empirical correlation functions may be developed between permeability and C44 for specific wells or formations based on data from accurate experimental measurements. Then the empirical relationship can be used to estimate permeability of that well or formation, or calibrate the permeability estimated from well log devices.
5. Shale samples are fragile and easy to break along the bedding plane, especially when it has experienced pressure increase and release procedures during the measurement. Both the velocity and permeability measurements are time-consuming. Therefore, consider the time efficiency, fragility of shale, and most importantly, the same in-situ condition to study the relationship between fluid flow and wave propagation in rocks. Finally, we assess that it is better to measure the permeability and ultrasonic velocity simultaneously under the same pressure and temperature conditions.

REFERENCES

Brace, W.F., Walsh, J.B., and Frangos, W.T., 1968, Permeability of granite under high pressure: Journal of Geophysical Research, 73, 2225-2236.

Bustin, R.M., 2005, Gas shales tapped for big play: AAPG Explorer, February.

Bustin, R.M., Bustin AMM, Cui X, Ross D.J.K, and Murthy Pathi V.S., 2008, Impact of shale properties on pore structure and storage characteristics, SPE Paper No. 119892-pp for Presentation at the 2008 SPE Shale Gas Production Conference, 16–18 November, Fort Worth, TX, USA.

Choquette P.W. and Pray L.C., 1970, Geologic nomenclature and classification of porosity in sedimentary carbonates. The American Association of Petroleum Geologists Bulletin, Vol. 54(2), Pgs. 207-244.

Civan, F., 2010a, Effective correlation of apparent gas permeability in tight porous media, Transport in Porous Media, Vol. 82, No. 2, pp. 375-384.

Civan, F., 2010b, A review of approaches for describing gas transfer through extremely tight porous media. in: The Third ECI International Conference on Porous Media and its Applications in Science, Engineering and Industry, Montecatini Terme, Italy, June 20-25.

Cui X., Bustin M.M.A., and Bustin R.M., 2009, Measuring of gas permeability and diffusivity of tight reservoir rocks: different approaches and their applications. Geo-fluids, 9:208–23.

Di Chen, 2012, Modeling Elastic Properties of Gas Shale and Microstructure Study on Barnett Shale, unpublished thesis (M.S.), University of Houston.

Dicker, A.I., and Smits, R.M., 1988, A practical approach for determining permeability from laboratory pressure-pulse decay measurements. SPE 17578.

Dyaur, N., Bayuk I., Mohamed Y., and Chesnokov, E., 2008, Anisotropy and elastic constants of the shale samples under unloaded conditions, 13th International workshop on Seismic Anisotropy.

Effective porosity. (n.d.). glossary.oilfield.slb.com. Retrieved November 1, 2012, from http://www.glossary.oilfield.slb.com/Display.cfm?Term=effective%20porosity.

Gale, J.F.W., R.M. Reed, and J. Holder, 2007, Natural fractures in the Barnett Shale and their importance for hydraulic fracture treatments. AAPG Bull., 91(4): 603-622.

Georgi D., Bespalov A., Tabarovsky L., Schoen J., 2002, On the relationship between resistivity and permeability anisotropy. Soc Pet Eng, paper SPE 77715.

Heinbockel, J. H., 2001. Introduction to Tensor Calculus and Continuum Mechanics: Trafford Publishing, Victoria.

Hornby, B. E., Schwartz, L. M., and Hudson, J. A., 1994, Anisotropic effective-medium modeling of the elastic properties of shales. Geophysics, 59, 1570–1583.

Hsieh PA, Tracy JV, Neuzil CE, Bredehoeft JD, 1981, A transient laboratory method for determining the hydraulic properties of tight rocks—I.Int J Rock Mech Min Sci. 18(3), 245–52.

Hubbert, M. K., 1957, Darcy's law and the field equations of the flow of underground fluids. Hydrological Science Journal, v. 2 p. 23-59.

Jones, L. E. A., and Wang, H. F., 1981, Ultrasonic velocities in Cretaceous shales from the Williston basin. Geophysics, 46, 288–297.

Javadpour, F., Fisher, D., and Unsworth, M., 2007, Nanoscale gas flow in shale gas sediments. Journal of Canadian petroleum Technology, 46, 55-61.

Deng, J., Wang, S., and Han, D., 2009, The velocity and attenuation anisotropy of shale at ultrasonic frequency. J. Geophys. Eng. 6 (2009) 269–278.

Jones, S.C., 1997, A technique for faster pulse-decay permeability measurements in tight rocks. SPE Formation Evaluation, 12(1):19.26. Paper SPE 28450.

Kamath J., Boyer R.E., and Nakagawa F.M., 1992, Characterization of core-scale heterogeneities using laboratory pressure transients. Paper SPE 20575 presented at the 65th Annual Technical Conference and Exhibition of the Society of petroleum Engineers held in New Orleans, LA, Sep. 23-26, 1990.

Kwon O., Kroneberg A.K., Gangi A.F., Johnson B., and Herbert B., 2004, Permeability of illite-bearing shale: anisotropy and effects of clay content and loading. J Geophys Res., 109, B10205, 19 p.

Lin W., 1982, Parametric analysis of the transient method of measuring permeability. J Geophys Res., 87, 1055–60.

Love, A. E. H., 1927, A Treatise on the Mathematical Theory of Elasticity, 4th edition, 643 pp., Cambridge Univ. Press, New York.

Luffel, D. L., Hopkins, C. W., and Schettler, P. D., 1993, Matrix permeability measurements of gas productive shales. Paper SPE 26633 presented at the 1993 SPE Annual Technical Conference and Exhibition, 3-6 October, Huston, TX, USA.

Metwally, Y.M., and Chesnokov, E., 2010, Measuring gas shale permeability tensor in the lab scale. SEG meeting. Denver. Technical Program. Expanded Abstract with Authors Biographies p.2628-2633.

Metwally, Y.M., and Chesnokov, E., 2011a, Gas shale; permeability-intrinsic parameters relationships. SEG meeting. San Antonio. Technical Program. Expanded Abstract with Authors Biographies. p. 4414-4419.

Metwally, Y.M., and Chesnokov, E., 2011b, Clay minerals transformation as a major source of authigenic quartz in thermally mature gas shale, Applied Clay Science, Doi:10.1016/j.clay.2011.11.007.

Metwally YM, Sondergeld CH., 2011, Measuring low permeabilities of gas-sands and shales using a pressure transmission technique. Int J. Rock Mech. Mining Sci, doi:10.1016/j.ijrmms.2011.08.004.

Pettijohn, F.J., 1975, Sedimentary Rocks, 3rd Edition, pp. 260 - 265.

Sayers, C. M., 1994, The elastic anisotropy of shales. J. Geophys. Res., 99, 767–774.

Schoenberg, M., 1994, Transversely isotropic media equivalent too thin isotropic layers, Geophysical Prospecting, 42, 885-915.

Sondergeld C. H., Rai C., Margesson R., and Whitten, K., 2000, Ultrasonic measurement of anisotropy on the Kimmeridge Shale, SEG meeting. Calgary. Technical Program. Expanded Abstract with Authors Biographies. p. 1858-1861.

Song I, Elphick S.C., Main I.G,, Ngwenya B.T., and Odling N.W., 2004, One-dimensional fluid diffusion induced by constant-rate flow injection: theoretical analysis and application to the determination of fluid permeability and specific storage of a cored rock sample. J. Geophy. Res., 109, paper B05207, doi:10.1029/2003JB002395.

Thomsen L, 1986, Weak elastic anisotropy. Geophysics, 51, 1954–66.

Trimmer D., 1981, Design criteria for laboratory measurements of low permeability rocks. Geophys. Res. Lett., 8(9), 973–5.

Vernik, L., Liu, X., 1997, Velocity anisotropy in shales: A petrophysical study,Geophysics, 521-532.

Wang, Z., 2002, Seismic anisotropy in sedimentary rocks, part 1: A single-plug laboratory method. Geophysics, 67, 1415–1422.

Wright H.M., Roberts J.J., and Cashman K.V., 2006, Permeability of anisotropic tube pumice: model calculations and measurements. Geophys. Res. Lett., 33, L17316

.

APPENDIX

A.1 Derivation of elastic property for TI medium (After Wang, 2002)

A TI medium has a hexagonal symmetry. It has five independence elastic constant. The relationship of stress and strain was established as blow,

$\sigma_i = C_{ij}\varepsilon_j$

$$= \begin{bmatrix} \sigma_1 \\ \sigma_2 \\ \sigma_3 \\ \sigma_4 \\ \sigma_5 \\ \sigma_6 \end{bmatrix} = \begin{bmatrix} C_{11} & C_{12} & C_{13} & 0 & 0 & 0 \\ C_{12} & C_{11} & C_{13} & 0 & 0 & 0 \\ C_{13} & C_{13} & C_{33} & 0 & 0 & 0 \\ 0 & 0 & 0 & C_{44} & 0 & 0 \\ 0 & 0 & 0 & 0 & C_{44} & 0 \\ 0 & 0 & 0 & 0 & 0 & C_{66} \end{bmatrix} \begin{bmatrix} \varepsilon_1 \\ \varepsilon_2 \\ \varepsilon_3 \\ \varepsilon_4 \\ \varepsilon_5 \\ \varepsilon_6 \end{bmatrix} \quad \text{(A-1)}$$

where σ_{ij} and ε_j are the stress and strain components and where C_{ij} is the elastic constant tensor. Although there are six constants in equation (A-1), only five constants are independent because $C_{66} = 1/2(C_{11} - C_{12})$. And the corresponding elastic velocities are

$$V_p = \sqrt{\frac{A+B}{2\rho}} \quad \text{(A-2)}$$

$$V_{s1} = \sqrt{\frac{A-B}{2\rho}} \quad \text{(A-3)}$$

$$V_{s2} = \sqrt{\frac{C_{66}\sin^2\theta + C_{44}\cos^2\theta}{\rho}} \quad \text{(A-4)}$$

where ρ is the bulk density, θ is the angle between the symmetry axis and the direction of wave propagation, and

$$A = C_{11}\sin^2\theta + C_{44} + C_{33}\cos^2\theta \quad \text{(A-5)}$$

$$B = \sqrt{[(C_{11} - C_{44})\sin^2\theta - (C_{33} - C_{44})\cos^2\theta]^2 + 4(C_{13} + C_{44})^2\sin^2\theta\cos^2\theta} \quad \text{(A-6)}$$

When $\theta = 0^o$, the waves are propagating parallel to the symmetry axis, which is perpendicular to bedding plane, so that

$$V_{p,0} = \sqrt{\frac{C_{33}}{\rho}} \qquad \text{(A-7)}$$

$$V_{S,0} = V_{S1,0} = V_{S2,0} = \sqrt{\frac{C_{44}}{\rho}} \qquad \text{(A-8)}$$

When $\theta = 90^o$, the waves are propagating perpendicular to the symmetry axis, which is parallel to bedding plane, then the velocities are

$$V_{p,90} = \sqrt{\frac{C_{11}}{\rho}} \qquad \text{(A-9)}$$

$$V_{s1,90} = \sqrt{\frac{C_{44}}{\rho}} \qquad \text{(A-10)}$$

$$V_{s2,90} = \sqrt{\frac{C_{66}}{\rho}} \qquad \text{(A-11)}$$

To calculate the P-wave and S-wave velocities at any angle of wave propagation, all five elastic constants and the bulk density must be known. Accordingly, the elastic constants can be calculated from five velocities (three compression and two shear) measured at three different angles and bulk density. Usually, we measure velocities at $\theta = 0^o$, and $\theta = 90^o$, (with equations (A-7)–(A-11)) and V_p at $\theta = 45^o$, therefore equations (A-2)–(A-6) can be derived in a relative simple form.

NOMENCLATURE

Greek

$\emptyset$	Porosity
ρ	Density
$\varepsilon,\ \gamma,\ \delta$	Thomsen's anisotropic parameters
μ	Viscosity
β	Compressibility
α	Slope
θ_n	n^{th} root of Eq. 3-12

Latin

A	Cross-section area
a	Ratio of sample pore volume to volume of upstream reservoir
b	Ratio of sample pore volume to volume of downstream reservoir
C	Elastic constant
g	Gravitational acceleration
K	Hydraulic conductivity
k	Permeability
L	Length

n	Direction cosine
P, p	Pressure
Q	Total discharge
q	Flow rate
S	Specific storage
T, t	Time
Vp	Compressional wave velocity
Vs	Shear wave velocity
V_B	Bulk volume
V_G	Grain volume
V_d	Volume of downstream reservoir
V_u	Volume of upstream reservoir
V_p	Pore volume
Z	Compressibility factor